Development of binary shaped pupil mask coronagraph for the observation of exoplanets

Kanae HAZE

DOCTOR OF
PHILOSOPHY

Department of Space and Astronautical Science
School of Physical Sciences
The Graduate University for Advanced Studies

2011

Contents

Abstract

Direct observation of extra-solar planets (exoplanets) is essential to understand how planetary systems were born, how they evolve, and ultimately, to identify biological signatures on these planets. However, the enormous contrast in flux between the central star and its associated planets is the primary difficulty in direct observation. Thus, the development of stellar coronagraphs, which can improve the contrast between the star and the planet, is needed. Of the various kinds of coronagraph, we have focused on a binary-shaped pupil mask coronagraph. The reasons for using this type of coronagraph are that it is robust against pointing errors, it can, in principal, make observations over a wide range of wavelengths and it is relatively simple. We conducted a number of coronagraphic experiments in a vacuum chamber using a checkerboard mask, which is a type of binary-shaped pupil mask, without active wavefront control.

1. We evaluated how much the PSF subtraction contributed to the high contrast observation by subtracting the images obtained through the coronagraph. We improved the temperature stability by installing the coronagraph optics in a vacuum chamber, controlling the temperature of the optical bench, and covering the vacuum chamber with thermal insulation layers. With a He-Ne laser at a wavelength of 632.8nm, a contrast of 2.3×10^{-7} was obtained for raw coronagraphic images and a contrast of 1.3×10^{-9} was achieved after subtraction of the PSF. Thus, an improvement of around two orders of magnitude in contrast was achieved by subtracting the PSF.

2. We also carried out multi-color/broadband experiments using Super luminescent Light Emitting Diodes (SLEDs) with center wavelengths of 650nm, 750nm, 800nm and 850nm in order to demonstrate that the binary-shaped pupil mask coronagraph could, in principal, be used for observations over a wide range of wavelengths. We achieved contrasts of 3.1×10^{-7}, 1.1×10^{-6}, 1.6×10^{-6} and 2.5×10^{-6} for the bands centered at 650nm, 750nm, 800nm and 850nm, respectively. The results show that the contrast within each wavelength band has been significantly improved compared with those obtained using non-coronagraphic optics.

3. However, the checker-board mask with a glass substrate has the problems of transmission losses, ghosting from residual reflectances and a slightly different refractive index for each wavelength. Therefore, we developed a new free-standing sheet metal mask without the need for a substrate.

> As a result, with the He-Ne laser and a free-standing mask, a contrast of 1.0×10^{-7} was achieved for the raw coronagraphic image by areal averaging of all the observed dark regions. Speckles are the major limiting factor. A similar significant improvement in contrast was demonstrated with a free-standing mask as with a substrate mask.

We demonstrated that subtraction of the PSF is potentially beneficial for improving the contrast of a binary-shaped pupil mask coronagraph, that this coronagraph can provide a significant improvement in contrast with multicolor/broadband light sources, and that the new free-standing mask for practical use provides superior performance of improving contrast. We performed the tasks necessary to make the coronagraph fit for practical use. In conclusion, we carried out verification tests on the binary-shaped pupil mask coronagraph for actual coronagraphic observations.

Chapter 1

Introduction

First, we shall describe the current situation with regard to the study of exoplanets and the motivation for our study (§1.1). After describing the importance and the difficulties of the direct observation of exoplanets, we will show that coronagraphs are essential for these studies (§1.2). Next, we shall review the various kinds of coronagraph and the previous studies done worldwide (§1.3). In §1.4, we explain our reasons for focusing on a binary-shaped pupil mask coronagraph from among the various kinds. We also show the working principle of, the advantages of and the previous studies done using binary-shaped pupil mask coronagraphs, and then, derive the problems which are absolutely essential for making the coronagraph fit for practical use. Additionally, the binary-shaped pupil mask coronagraph has the potential to be used for the SPICA coronagraph (§1.5). Finally, we set out the purpose of this thesis, which is to perform the tasks necessary to make the coronagraph fit for practical use (§1.6).

1.1 Exoplanet

Since the discovery of the extra-solar planet (exoplanet), 51 Pegasi b, in 1995 (Mayor & Queloz, 1995), more than 700 exoplanets have been found. A study of exoplanets is essential for understanding the evolution of and the variety in planetary systems, and, ultimately, for finding biological signatures of these planets. Most exoplanets so far discovered are massive gas giant planets which have planetary orbits quite unlike those in our Solar System. We have learned that the planetary systems are very diverse (e.g., eccentric orbits, Hot Jupiters and Hot Neptunes). Studies of exoplanets are complementary to the studies of planets in our solar system and are essential for understanding the variety and evolution of planets. However, the enormous contrast in luminosity between the central star and the planet presents the primary difficulty in the direct observation of exoplanets (Fig. 1.1).

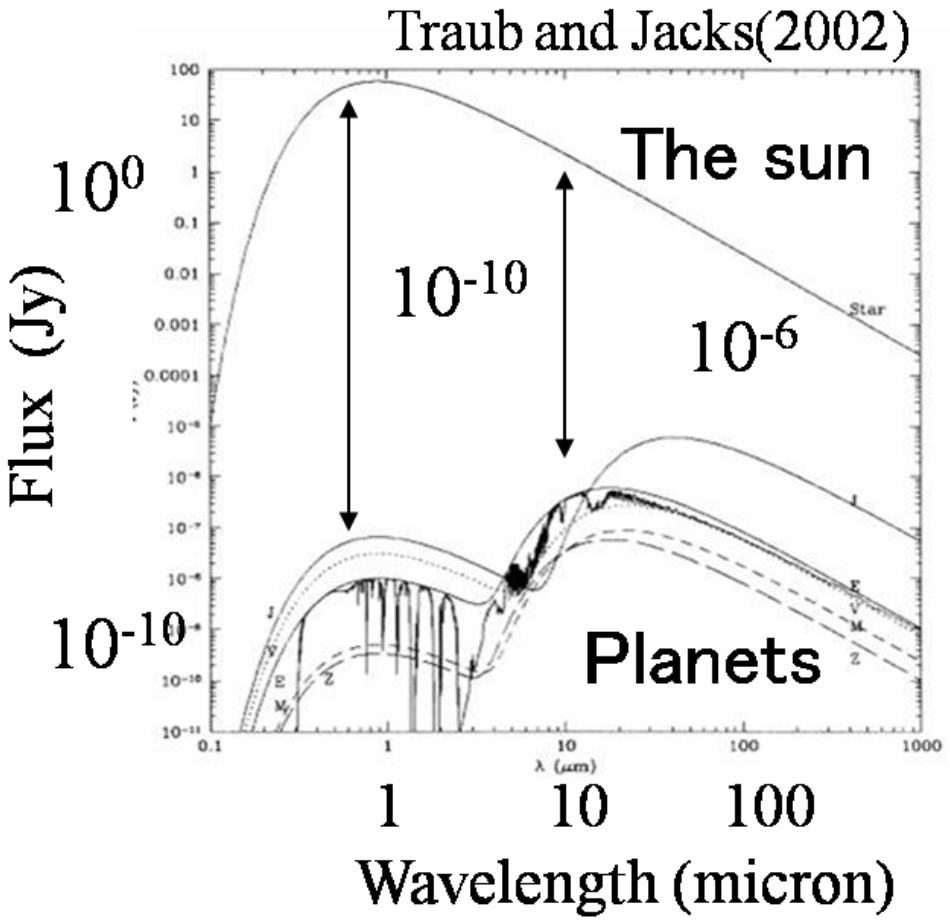

Figure 1.1: Solar system blackbody thermal emission spectra and reflected light spectra at 10 pc, for the Sun, Jupiter (J), Earth (E), Venus (V), Mars (M), and zodiacal dust (Z).

1.1.1 Previously-discovered planets

Our sun has eight planets. In order of distance from the sun these are Mercury, Venus, Earth, Mars, Jupiter, Saturn, Uranus and Neptune. Mercury, Venus, Earth and Mars are terrestrial planets which have a layered structure with an iron core and a rocky mantle. Jupiter and Saturn are gas-giant planets which have a core mostly of ice ($< 20M_{\oplus}$[†]) with H and He gases surrounding the core. Uranus and Neptune are considered to consist almost entirely of ice. Each of the planetary orbits are near-coplanar circular orbits (eccentricity: e < 0.1).

On the other hand, most exoplanets discovered so far are massive gas giant planets which have very small orbits, such as Hot Jupiters, and planets in elliptical orbits with large eccentricities, such as eccentric planets. Exoplanets have different orbital radii, eccentricity and planetary mass distribution from those in our solar system.

1.1.2 Conventional observation methods

We want to acquire data about planets orbiting stars of various mass and at different evolutionary stages, but the information we have is somewhat biased. There are planets that cannot be detected because the conventional methods of observation have limitations. This is a big problem in studying the diversity and the evolution of exoplanets. The conventional observation methods and their limitations are as shown below.

Radial velocity observations

Since the discovery of the exoplanet, 51 Pegasi b, in 1995 (Mayor & Queloz, 1995), many exoplanets have been detected through radial velocity observations. This method is to measure the radial velocity of the star, which is affected by the orbital motion of the planet. The velocity vector of the star can be deduced from the displacement in the spectral line from it due to the Doppler effect. Additionally, we can find the orbital radius from the stellar mass and the period, which are observable quantities. We can only deduce a lower limit for the planetary mass from the orbital radius and the radial velocity. The Doppler shift can be observed only from a bright star which is relatively close to the sun. This is because a high-dispersion spectrum is necessary to detect the Doppler shift. Doppler shifts in stellar spectra have been measured to an accuracy of about 3m/s, although 10m/s is common, and 1m/s may be the ultimate limit of this technique. By comparison, the solar velocity due to Jupiter is about 3m/s, and that due to Earth is about 0.01m/s. However the Doppler shift cannot be detected from a massive star even if it is a bright star, because of the too small variation. Only a period which is shorter than, or equal to, the data acquisition time can be detected. This is because an observation time longer than the planetary period is necessary in order to detect variations in the radial velocity.

[†] $M_{\oplus}$ is the mass of the earth ($6.0 \times 10^{27} g$).

Transiting planet observations

If the planet's orbital plane is seen nearly edge-on, a partial eclipse of the star by the planet may occur. The transit method measures planetary extinction (Charbonneau et al., 2000). Precise photometry allows us to infer the stellar limb darkening, the orbital radius of the planet, the inclination of the orbit, and therefore the planet's mass. Not only detection but also spectroscopic studies of some transiting exoplanets have been carried out (e.g., Deming et al. (2005); Tinetti et al. (2007); Swain et al. (2009)). A primary eclipse occurs when the planet passes in front of the star. Light transmitted from the planetary atmosphere can be obtained by comparing the stellar spectra when the planet passes in front of the star with that when it doesn't. A secondary eclipse occurs when the planet passes behind the star. If we subtract the stellar spectra from the spectrum of the star and planet, we can detect infrared light from the planetary atmosphere. For example, extinction between the Sun and Jupiter can be detected with a photometric accuracy of one percent or less because the cross-section ratio is 1/100. The transit method doesn't require a large-scale instrument. Thus, a telescope of several dozen meters and a commercially available CCD camera will suffice. The limiting conditions for the observation are that the planet's orbital plane must be seen nearly edge-on, and that we can only make observations while the planet transits the star.

Gravitational microlensing observations

If an object in the foreground is aligned between the Earth and a bright star, the light from the background star is bent by the mass of the foreground object and can be detected by an increase in luminosity. This is called gravitational microlensing, as the foreground object acts like a lens. Additional observations are not possible because this event happens only once per object. The first exoplanet to be discovered by microlensing was in 2004 (Bond et al., 2004). With microlensing faint planetary mass objects (e.g., Earth-mass planets) which are either unbound to any host star or are in very large orbits, can be detected because the lens object is detected by means of its mass and not its luminosity. The gravitational lensing method is complementary to those other methods of observation. So far thirteen exoplanets have been discovered by this method with two of them being about $3 - 6M_{\oplus}$ (Beaulieu et al. (2006); Bennett et al. (2008)).

1.1.3 Selection effects

The vast majority of exoplanets detected so far have large mass. This is largely due to an observational selection effect, because all the detection methods are much more likely to discover massive planets. Most planets have been discovered around main sequence stars (F, G and K stars). Those around A and B stars in the main sequence can't be detected using the radial velocity method, because the shift of a massive star is very small. The radial velocity method can be used for detecting the shift of an M star that is in the immediate vicinity of

the sun, because an M star is faint. An M star can be detected by gravitational microlensing, although the number of planets detected is small. Furthermore, additional observations are not possible because the gravitational microlensing event happens only once per object. We can detect only short-period gas-giant planets which have small orbital radii by these methods. Exoplanets can be detected by the transit method only when the orbital plane is nearly edge-on to our line of sight.

Much less information can be obtained about exoplanets from indirect methods than from direct methods, because indirect methods do not make observations of the exoplanet itself. We have been directly observing only young planetary systems in which the planets are far from the central star, because the contrast between the planet and the star is small and it is easy to separate the planetary light from the stellar light.

1.1.4 Problems with previous exoplanet observations

Previous observations have revealed the existence of many exoplanets which are far different from those in our solar system. However, the observations still lack detail and are far from systematic. There are two problems.

- One is the lack of information about the planet itself. We have little information obtained by light from a planet itself (e.g., spectroscopic data) because most of the previous observations are indirect observations.
- The other is the observational selection effect. Most planets observed so far are short-period gas-giant planets which have been discovered around main sequence stars (F, G and K star).

Additionally, more detailed and systematic data is required to construct a generalized theory of planetary formation.

1.2 Direct observations of exoplanets

1.2.1 Importance of direct observations

Direct observations (imaging and spectroscopy) of exoplanets help us to gather detailed information, such as the size, color, luminosity and atmospheric spectrum of the planet. For instance, referring to Fig.1.2, it is expected that the Spectral Energy Distribution (SED) of Jovian exoplanets can be obtained (Burrows et al., 2003). Wavelength coverage from MIR to 3.5μm allows us to study interesting molecular features of the planetary atmospheres, e.g., H_2O, CH_4, NH_3. Broadband spectroscopy of exoplanets is expected to play an important role in revealing these spectral features of the planetary atmospheres. Also, we expect to be able to make new discoveries (e.g., exoplanets having larger orbital radii, planets around AB and M type stars), which were not possible previously because of the observational selection effect. Therefore, direct observation is critical for understanding the evolution and variety of planetary

systems. The detailed information obtained from direct observations can be used together with information obtained from indirect observations to achieve this understanding.

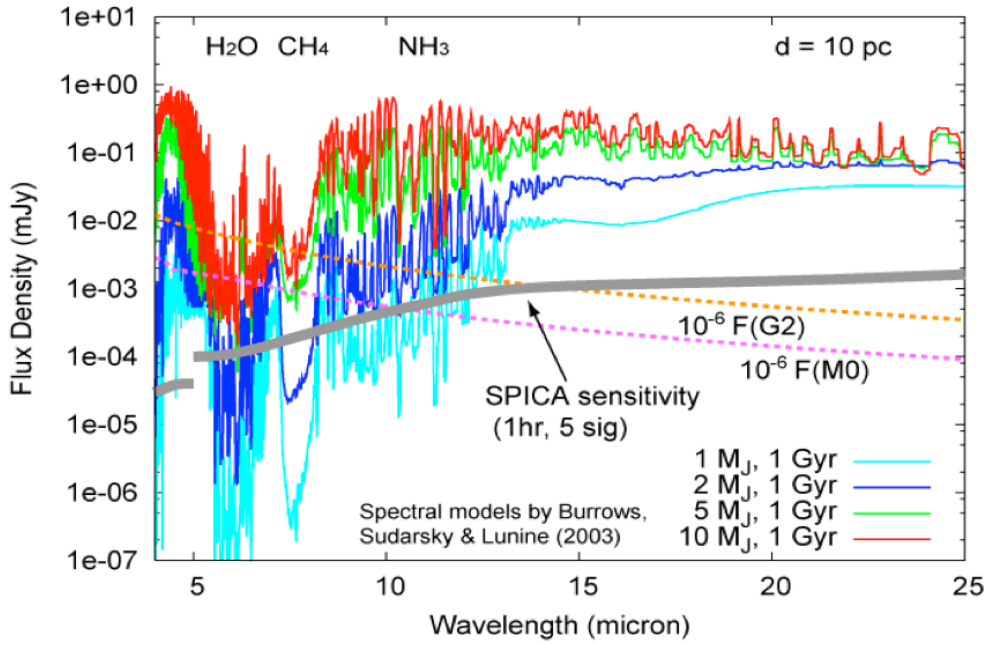

Figure 1.2: Calculated SEDs of 1Gyrs old Jovian planets with various masses and properties relating to SPICA observations. 10pc is assumed as the distance to the planetary system. The gray solid curve shows the limit to the sensitivity for imaging with SPICA. The orange and purple dashed lines show the scaled SEDs of G2 and M0 type stars, respectively. This figure is from Enya et al. (2010).

1.2.2 Difficulties of direct observations

The direct detection and spectroscopy of exoplanets is essential for understanding how planetary systems were born, how they have evolved, and, ultimately, for finding the biological signatures of these planets. The enormous contrast in luminosity between the central star and a planet presents the primary difficulty in the direct observation of exoplanets. For example, if a solar system is observed from a distance, the expected contrast between the central star and the planet at visible light wavelengths is $\sim 10^{-10}$ but is reduced to $\sim 10^{-6}$ in the mid-infrared region (Traub & Jucks, 2002), as shown in Fig. 1.1. In this case, it is difficult to make direct observations with an ordinary telescope because the planet is buried in the halo of the central star image.

Recently, some studies on direct observations were presented (e.g., Marois et al. (2008); Kalas et al. (2008)), but only on young gas-giant planets very far from the central star.

1.3 Coronagraphs

One of the ways in which the enormous contrast can be improved is to use a stellar coronagraph. Firstly, the coronagraph is evaluated for solar observations (Lyot, 1939), and this can have special optics to improve the contrast by minimizing the effect of diffracted light from the central star. This is not done by blocking the light, but controlling the Point Spread Function (PSF), as shown in Figure 1.3. The coronagraph can change the PSF and reduce the luminosity gap between an exoplanet and its central star. By developing a stellar coronagraph, we expect to detect the planet beyond the observable limit and obtain planetary information, such as its color, shape, size, atmospheric spectrum and so on. There are various kinds of coronagraph, such as a Lyot-type Coronagraph(Lyot, 1939), a Phase shifting Mask Coronagraph(Roddier & Roddier, 1997; Rouan et al., 2000) , a Pupil-plane Mask Coronagraph (Jacquinot & Roizen-Dossier, 1964) and a Phase Induced Amplitude Apodization (PIAA) Coronagraph(Guyon, 2003).

Experimental demonstrations are necessary because the theory is ahead of the experiments, and the experiments conducted need to have a high accuracy to enable the theory to be demonstrated. Thus, a development race is being conducted worldwide (e.g., Guyon et al. (2006), see their Table1). In this section, we describe the concepts of some coronagraphs and ongoing laboratory testing for space-telescopes.

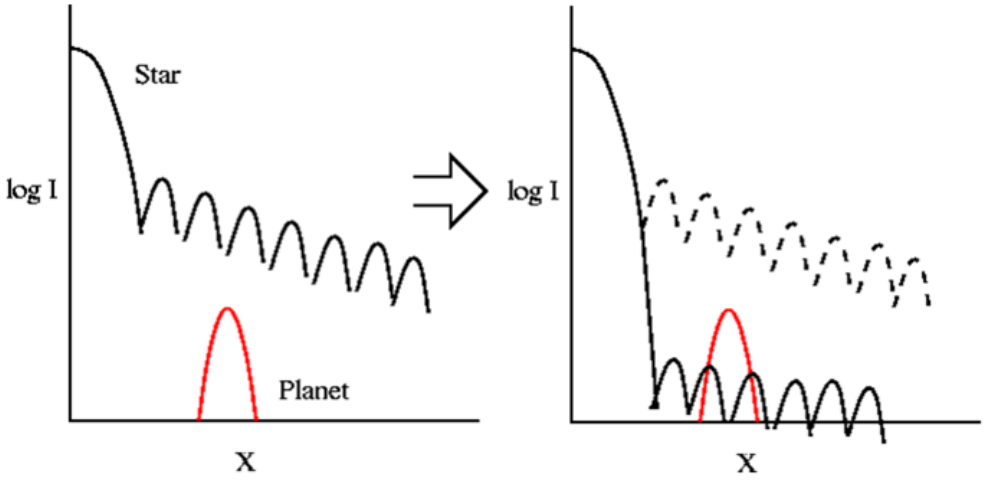

Figure 1.3: The coronagraph can minimize the diffracted light from the central star.

Lyot-type Coronagraph As shown in Fig.1.4, this coronagraph can reduce the stellar flux by placing a focal-plane mask (e.g., an occulting spot) in the first focal plane and the Lyot stop, which blocks out the remaining rings of light from the central star while allowing most of the light from surrounding sources to pass through to the final image, on the

next pupil plane.

Improved performance over the original Lyot design can be obtained by, for example, the following methods: the Apodized Pupil Lyot Coronagraph (APLC), the band-limited coronagraph (BL), the Phase Mask coronagraph (PM), the Four Quadrant Phase Mask coronagraph (FQPM) and the Optical Vortex Coronagraph (OVC).

The Amplitude mask coronagraphs (APLC, BL) operate on the intensity of light in the focal plane, and not on the phase. The APLC described in Soummer et al. (2003), where the entrance pupil of a Lyot coronagraph with a hard edged focal plane occulter is optimally apodized. A slightly different approach, explored by Vanderbei et al. (2004, see their Fig.3), is to apodize the pupil after the hard edged focal plane occulter. As suggested by Aime & Soummer (2004), the output of an APLC can be used as the input of a second stage APLC: these are the multistep APLCs. The BL uses a special kind of mask called a "band-limited mask" in the focal plane. This mask is designed to block light and also manage diffraction effects caused by the removal of the light (e.g., Kuchner & Traub (2002); Kuchner et al. (2005)).

On the other hand, the Phase mask coronagraphs (PM, FQPM, OVC) introduce Phase shifts in the focal plane. The PM coronagraph (Roddier & Roddier, 1997) uses a circular-shifting focal plane mask, and a mild pupil amplitude apodization (Guyon & Roddier, 2000; Soummer et al. , 2003). The FQPM (Rouan et al., 2000) uses a focal plane mask that shifts two out of four quadrants of the image by π. The achromatic phase knife coronagraph (Abe et al., 2001) is another form of FQPM. In the OVC (Palacios, 2005; Foo et al., 2005; Swartzlander, 2006) and the Angular Groove Phase Mask Coronagraph (AGPMC) (Mawet et al., 2005), a focal plane vortex phase mask replaces the four-quadrant phase mask of the FQPM, thus avoiding the "dead zones" of the FQPM. In (r, θ) polar coordinates, the mask phase is equal to mθ, where m is the topological charge.

Phase Mask laboratory testing: Monochromatic device performance has already been demonstrated and the manufacturing procedures have been well-under control since their development. Among them, the AGPMC (Mawet et al., 2005; Foo et al., 2005), the FQPM (Carlotti et al., 2009) , and the Eight-Octant Phase Mask (EOPM) (Murakami et al., 2008) are quite promising. The multistage FQPM reduces the stellar flux over a spectral range and it is a very good candidate to be associated with a spectrometer for future exoplanet imaging instruments in ground- and space-based observatories (Baudoz et al., 2008). The coronagraph gives an average transmission between 7×10^{-6} and 4×10^{-5} at each wavelength

over a 20% bandwidth (660-800 nm) (Galicher et al., 2011).

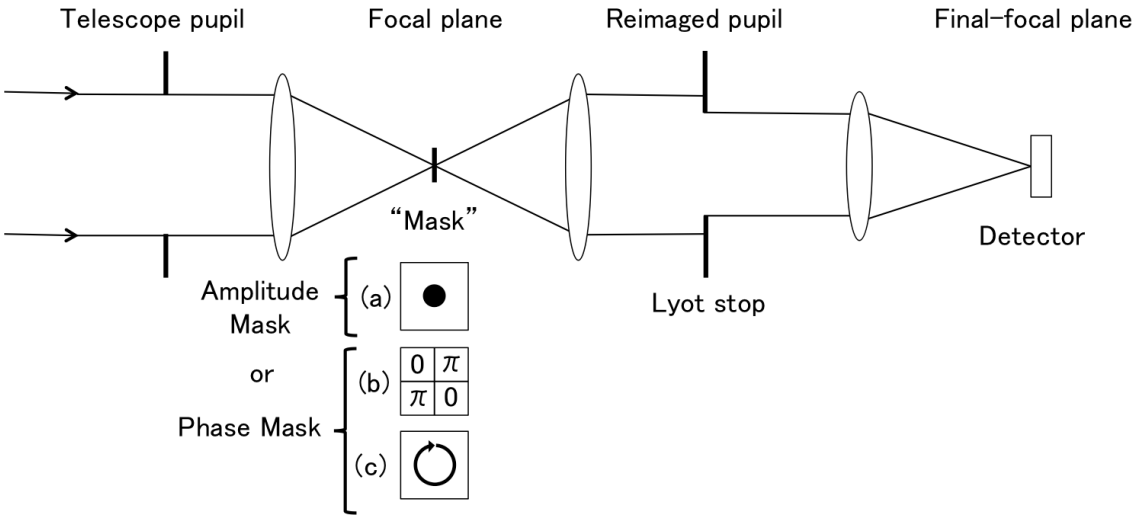

Figure 1.4: Concept of the Lyot coronagraph. There are various kinds of Lyot-type coronagraph including ones with Amplitude or Phase masks, such as (a) the occulting mask, (b) the Four Quadrant Phase Mask, and (c) the optical vortex mask, in the focal plane.

Pupil-plane Mask Coronagraph The complex amplitude at the pupil can be modified to yield a PSF suitable for high-contrast imaging, a property used by many coronagraph concepts. Apodization can be performed by a pupil plane amplitude mask (Conventional Pupil Apodization, or CPA), which can be continuous or binary (Jacquinot & Roizen-Dossier, 1964; Nisenson & Papaliolios, 2001; Spergel, 2001; Gonsalves & Nisenson, 2003; Kasdin et al., 2003, 2005a,b; Aime, 2005; Vanderbei et al., 2003a,b, 2004; Green et al., 2004; Tanaka et al., 2006; Carlotti et al., 2011; Enya & Abe, 2010; Enya et al., 2011), as shown in Fig.1.5. Apodization by Mach-Zehnder type pupil plane interferometry has also been suggested by Aime (2001) to produce a continuous apodization. If only one-half of the focal plane is considered, amplitude pupil apodization can be replaced by phase-only apodization (pupil phase apodization, or PPA), just as phase corrections in the pupil can only cancel focal plane speckles in one-half of the field of view. High-contrast imaging with phase apodization was proposed by Yang & Kostinski (2004), who found solutions for broad-band imaging and obtained contrast/throughput performances similar to amplitude apodization designs (although only over a quarter of the field of view). Codona & Angel (2004) independently computed a PPA solution for the Hubble Space Telescope pupil to suppress diffraction in half of the field of view.

Pupil-plane Mask Coronagraph laboratory testing: Belikov et al. (2006) achieved a contrast of 4×10^{-8} using a visible laser, and a contrast of

$\sim 10^{-7}$ using a broadband light source with speckle nulling in a small area from $4\lambda/D$ to $9\lambda/D$. The details of the Pupil-plane Mask Coronagraph are discussed in section 1.4.

PIAA Coronagraph As shown in Fig.1.6, this coronagraph uses lossless amplitude apodization of the pupil performed by geometric redistribution of the light rather than selective absorption (Guyon, 2003; Traub & Vanderbei, 2003; Guyon et al., 2005; Vanderbei & Traub, 2005; Martinache et al., 2006; Vanderbei, 2006; Pluzhnik et al., 2006).

PIAA laboratory testing: The laboratory experiment achieved a raw contrast of 2.27×10^{-7} between 1.65 λ/D (inner working angle of the coronagraph configuration tested) and 4.4 λ/D (outer working angle) (Guyon et al., 2010). The NASA Ames Research Center PIAA coronagraph laboratory is a highly flexible testbed operating in air (Belikov et al., 2009). It is dedicated to PIAA technologies and is ideally suited to rapidly developing and validating new technologies and algorithms. It uses MEMS-type deformable mirrors for wavefront control. The NASA JPL High Contrast Imaging Testbed (HCIT) is a high stability vacuum testbed facility for coronagraphs. PIAA is one of the coronagraph techniques tested in this lab, which provides the stable vacuum environment ultimately required to validate PIAA for flight (Kern et al., 2009) .

There are many various kinds of coronagraphic experiments which have different purposes and demonstrate different performance.

1.4 Binary-shaped pupil mask coronagraph

Of the various kinds of coronagraph, we have focused on a binary-shaped pupil mask coronagraph. The reasons for using this coronagraph are that it is robust against pointing errors, can, in principal, make observations over a wide range of wavelengths and is relatively simple (Jacquinot & Roizen-Dossier, 1964; Spergel, 2001; Vanderbei et al., 2003a,b, 2004; Kasdin et al., 2003, 2005a,b; Green et al., 2004; Tanaka et al., 2006; Enya & Abe, 2010; Enya et al., 2011).

First, we refer to the principle of pupil apodization and the binary-shaped pupil masks coronagraph. In this paper, we assume that the telescope optics follow the Fraunhofer approximation. Hence, given a pupil-plane apodization function $0 \leq A(x, y) \leq 1$, the image-plane electric field corresponding to an on-axis point source is given by the two dimensional Fourier transform of the apodization function:

$$E(\xi, \zeta) = \int\int e^{2\pi i(\xi x + \zeta y)} A(x, y) dx dy, \tag{1.1}$$

where $E(\xi, \zeta)$ is the magnitude of the electric field, ξ and ζ are the coordinates on the image plane, x and y are the coordinates on the pupil plane,

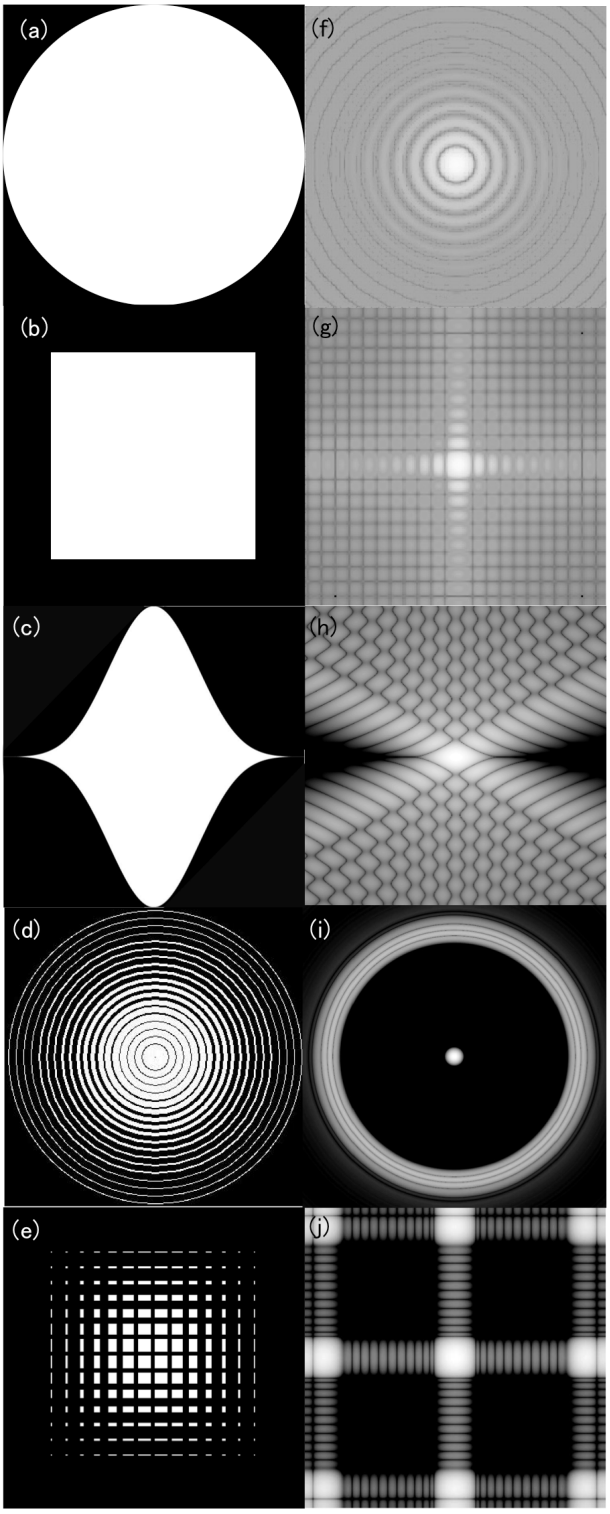

Figure 1.5: Panels (a), (b), (c), (d) and (e) show the binary-shaped pupil mask designs. (a) is a circular aperture, (b) is a rectangular aperture, (c) is a single prolate spheroidal wave function shaped-pupil mask, (d) is a ring shaped pupil mask and (e) is a checkerboard pupil mask. The transmission through the black and white regions is 0 and 1, respectively. Panels (f), (g), (h), (i) and (j) show the expected (theoretical) PSFs for (a), (b), (c), (d) and (e), respectively. The gray scale is logarithmic. Panels (c), (d), (h) and (i) are from Kasdin et al. (2003). Panels (e) and (j) are from Vanderbei et al. (2004).

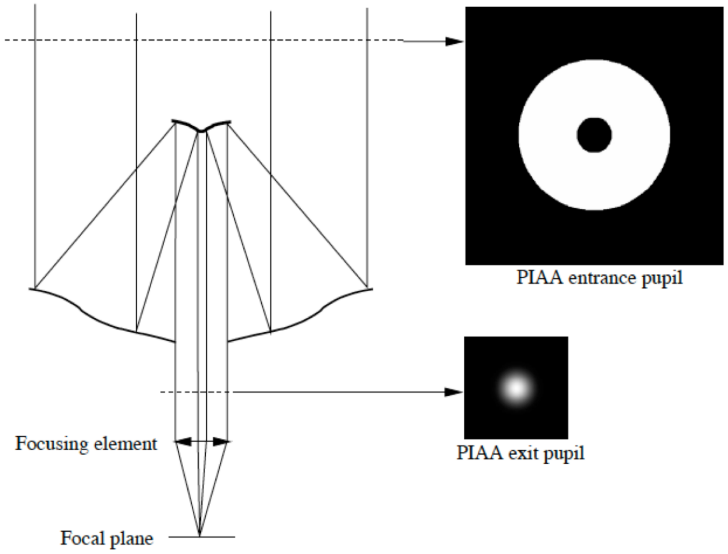

Figure 1.6: Schematic representation of the PIAA technique from Guyon (2003).

and A(x,y) is the apodization function. If the apodization function takes only the values zero and one, then the function represents a "binary-shaped pupil mask". The intensity in the image plane is the square of the magnitude of the electric field. This intensity function is called the PSF. Certain performance metrics guide our choice of the best pupil apodization or binary-shaped pupil mask. For comparison purposes, we review these metrics for some binary-shaped pupil masks, as shown in Fig. 1.5. There are various kinds of binary-shaped pupil mask, such as a Gaussian pupil mask (Spergel, 2001; Kasdin et al., 2003), a ring shaped pupil mask (Vanderbei et al., 2003a; Green et al., 2004), and a checkerboard pupil mask (Vanderbei et al., 2004; Tanaka et al., 2006). These coronagraphs can make a "dark region", which is the area in which diffracted light from the central star is reduced.

Second, we compare the Lyot-type coronagraph and the binary-shaped pupil mask coronagraph in order to describe the benefits of the binary-shaped pupil mask coronagraph. The Lyot-type coronagraph achieves a high-contrast by placing the mask in the focal plane; on the other hand, the Binary-shaped pupil mask coronagraph achieves a high-contrast by placing the mask in the pupil plane. Therefore, the binary-shaped pupil mask coronagraph is robust against pointing errors compared with the Lyot-type coronagraph. Furthermore, the Lyot-type coronagraph requires the mask position to be shifted with wavelength, but the binary-shaped pupil mask coronagraph does not. The binary-shaped pupil mask coronagraph can make observations over a wide range of wavelengths. Note that the size of the PSF scales with wavelength. Thus, this coronagraph has the advantages of being robust against pointing errors and can, in principal, be used for observations over a wide range of

wavelengths.

Finally, we refer to laboratory testing of a checkerboard mask coronagraph. There are a variety of binary-shaped pupil mask coronagraphs which have different mask patterns, as shown in Fig.1.5. Among these, we chose a checkerboard mask coronagraph (e.g., Figs.1.5 (e)and(j)). The reason is that the checkerboard mask has some advantages over other masks in the manufacturing of the mask. One reason is that the mask pattern is relatively easy to make using microfabrication technology. A checkerboard pattern consisting of rectangular shapes is easier to make than a Gaussian pupil mask (Figs.1.5 (c)) using microfabrication technology. The second reason is that the checkerboard mask design can be made as a free-standing mask without a substrate. A ring shaped mask (Figs.1.5 (d)) is not suitable for a free-standing mask. It should be noted that the principle of the barcode mask was presented by Kasdin et al. (2005a), and the LOQO optimizer presented by Vanderbei (1999) was used for optimization in these designs. The first demonstration experiments with the checkerboard pupil mask were carried out by Enya et al. (2007). The size of the mask used for the experiments was 2mm.

Enya et al. (2007) presented the first results from their experiments involving a coronagraph with a checkerboard pupil mask, as shown in Figure1.7, without AO at room temperature in air. Two masks, consisting of aluminum films on a glass substrate, were manufactured using nano-fabrication techniques with electron beam lithography: Mask 1 was optimized for a pupil with a 30% central obstruction and Mask 2 was for a pupil without obstruction. The theoretical contrast for both masks was 10^{-7} and no AO system was employed. For both masks, the observed PSFs were quite consistent with the theoretical ones, as shown in Figure1.7 and Figure1.8. Contrasts of 2.7×10^{-7} for Mask 1 and 1.1×10^{-7} for Mask 2 were achieved for raw coronagraphic images in Figure1.8. These contrasts are better than 10^{-6} which is the contrast between the sun and the planets at infrared wavelengths. Bright speckles are caused by a combination of effects in the beam-line: wavefront errors(WFE), multi-reflections and scattering by microscopic defects on the surface of the optics and can therefore be reasonably considered as being limiting factors in this experiment.

In the previous experiments, the high contrast performance ($< 10^{-6}$) of the binary-shaped pupil mask coronagraph was confirmed. Further development and verification are required to install a binary-shaped pupil mask coronagraph on a telescope. In space telescopes, the WFE caused by imperfections in the optics is an important limiting factor in the contrast of a coronagraph. For an actual observation, it is necessary to make observations over wavelength bands, and it would be beneficial to make observations using multiple bands. A checkerboard mask with a glass substrate has the problems of transmission losses, ghosting from residual reflectances and a slightly different refractive index for each wavelength. Dealing with these problems is absolutely essential for making the coronagraph fit for practical use.

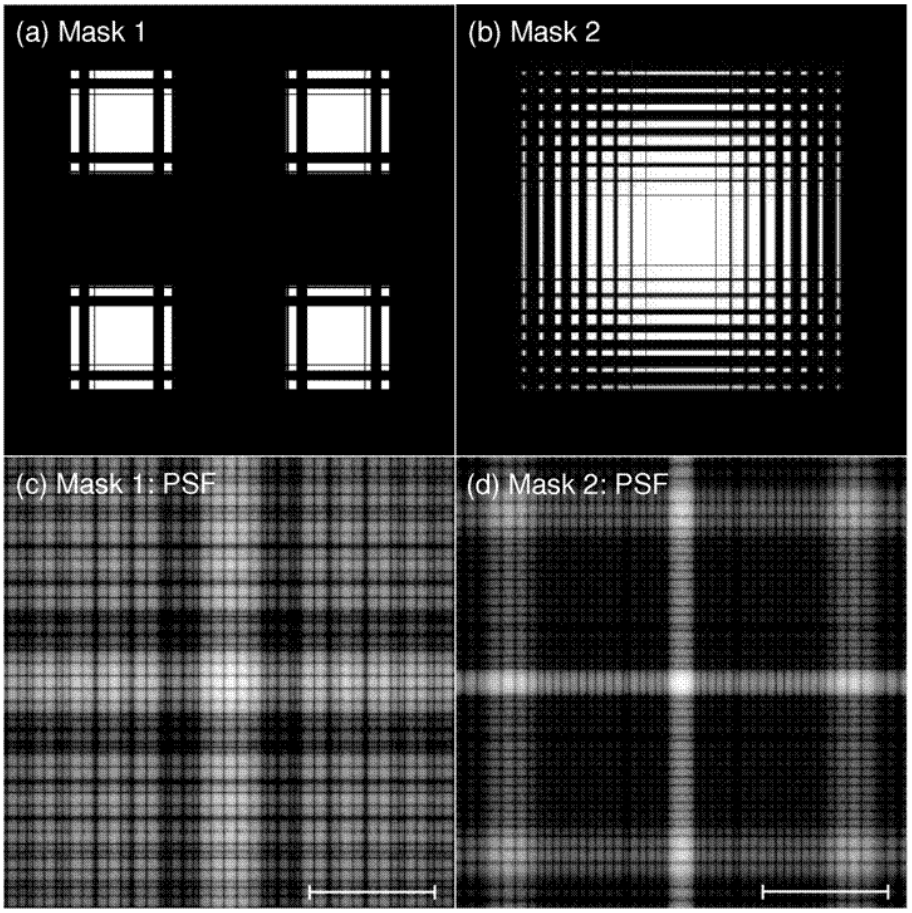

Figure 1.7: Panels (a) and (b) show the Mask 1 and Mask 2 designs. The transmission through the black and white regions is 0 and 1, respectively. The diameter of the circumscribed circle to the transmissive part is 2mm. Panels (c) and (d) show the expected (theoretical) PSFs for Masks 1 and 2. The scale bar is $20\lambda/D$. Fig.1 is from Enya et al. (2007).

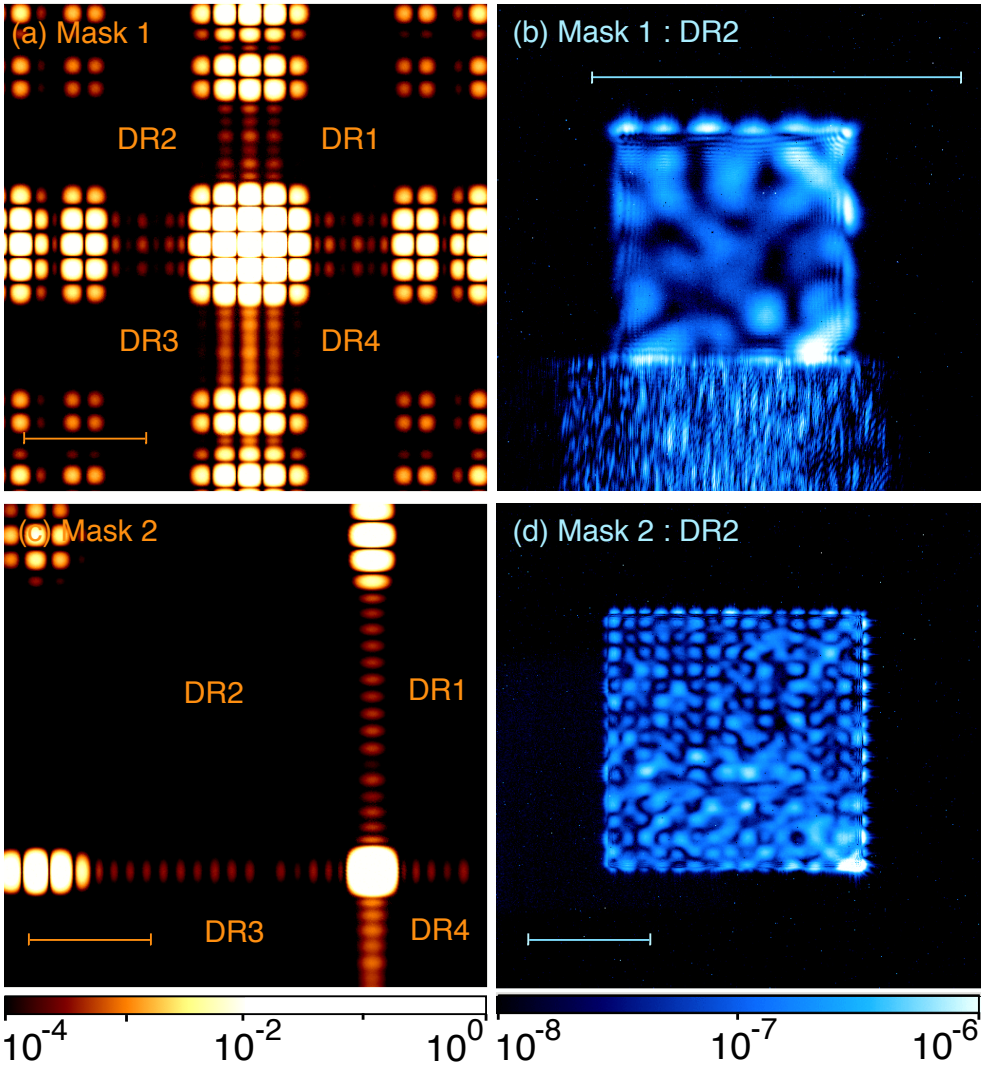

Figure 1.8: Panels (a) and (c) show images including the core of the PSF for Mask 1 and Mask 2. The tail below the bright peak is due to a readout effect. Panels (b) and (d) are images of the dark regions obtained with a mask with a square aperture. The prickle like pattern below the square aperture in (b) is the result of reflection by the support structure of the aperture for Mask 1. The scale bar is $10\lambda/D$. Fig.2 is from Enya et al. (2007).

1.5 SPICA coronagraph

There is a plan to install a stellar coronagraph in the Space Infrared telescope for Cosmology and Astrophysics (SPICA). SPICA (2018 launch planned) is an astronomical mission optimized for mid-infrared and far-infrared astronomy with a 3m class on-axis telescope cooled to <6K (Nakagawa et al., 2010). The primary target of the SPICA coronagraph is self-luminous Jovian exoplanets around 1-5 Gyr old G-M type stars. The binary shaped pupil mask coronagraph has the potential to be used for the SPICA coronagraph (Enya et al., 2010).

The SPICA coronagraph has several unique features. First of all, it targets not the visible region but the mid-infrared region. The mid-infrared region has a great advantage in direct observations, because the contrast between the sun and the planets is $\sim 10^{-6}$ in the mid-infrared region, whereas it is $\sim 10^{-10}$ in the visible region (Fig. 1.1), as previously described. Secondly, it is a space telescope. Space-borne telescopes have an advantage as platforms for high contrast coronagraphs because they are free from air turbulence and atmospheric infrared absorption. Thirdly, it is a cryogenic telescope. Cryogenic telescope provides high sensitivity in the infrared region. High stability is expected as the cryogenic telescope is to be launched into deep space, the Sun-Earth L2 Halo orbit. In addition, the structure of the SPICA telescope, adopting a monolithic primary mirror and carefully designed secondary support, yields a clean point spread function (PSF). Therefore, the SPICA coronagraph provides a great opportunity for systematic exoplanet observations.

1.6 Purposes of this thesis

The purpose of this thesis is to perform the tasks necessary to make the coronagraph fit for practical use, as described below.

1. Subtraction of the PSF is advantageous in that it removes any static WFE, and achieves a higher contrast than the raw contrast of the coronagraph (Trauger & Traub (2007)). In space telescopes, the WFE caused by imperfections in the optics is an important limiting factor in the contrast of a coronagraph. PSF subtraction is available in direct observations of exoplanets using space telescopes, which helps to improve high-contrast observations. We evaluate how much the PSF subtraction contributes to high contrast observations by subtracting the images obtained through the coronagraph.

2. A He-Ne laser was employed as the light source in the previous experiments. For an actual observation, it is necessary to make observations over a wavelength band, and it would be beneficial to make observations using multiple bands. In principle the binary-shaped pupil mask coronagraph should work at all wavelengths. We demonstrate this by changing

the experimental system from a He-Ne laser source to broadband and multi-band light sources.

3. However, the checker-board mask with a glass substrate has the problems of transmission losses, ghosting from residual reflectances and a slightly different refractive index for each wavelength. Therefore, we have developed a new free-standing mask with sheet metal without a substrate and we demonstrate the contrast performance. The free-standing mask is available for infrared observations, which have a great advantage over visible light observations in that the contrast between the star and the planet.

This study is unique and important in that it includes not only the tasks necessary to make the coronagraph fit for practical use, but also tests to verify its use for actual coronagraphic observations.

An outline of this paper is as follows. In the next section "Experiments and Results", we present three kinds of experiment, concerning 1, 2, and 3 as above. We describe the common part of the three experiments and then describe separately each of the three experiments and the results, and present a discussion of each. In the third section, "Discussions", we discuss the issues mentioned above and the results from a combination of the experiments.

Chapter 2

Experiments and Results

In this section, we present three kinds of experiment, a PSF subtraction experiment, a multi-color/broadband demonstration and free-standing mask experiments. We describe the common part of the three experiments and then describe each separately.

2.1 High dynamic range Optical Coronagraph Testbed (HOCT)

Fig.2.1 shows the experimental platform, called the HOCT, used for this work. All the experimental optics were located in a clean-room at the Institute of Space and Astronautical Science/ Japan Aerospace Exploration Agency (ISAS/JAXA). The coronagraphic optics were set on an optical bench in a vacuum chamber. The optical bench was set on supports consisting of glass epoxy plates. We used a He-Ne laser with a wavelength of 632.8nm and Super luminescent Light Emitting Diodes (SLEDs) with center wavelengths of 650nm, 750nm, 800nm and 850nm, as light sources (Table 2.2). Light passes into the chamber through a single-mode optical fiber. The entrance beam from the optical fiber is collimated by a 50mm diameter BK7 plano-convex lens (SIGMA KOKI CO., LTD.), and the collimated beam passing through the pupil mask is focused by a second plano-convex lens. Active wavefront control is not applied in this work. A bi-convex lens is used to reproduce the image through a window in the chamber. SIGMA KOKI CO., LTD. is able to routinely achieve a surface accuracy of $\lambda/10$ for the window and 2.5λ for the lenses. Broadband multiple-layer anti-reflection (BMAR) coatings optimized for wavelengths of 400-700 μm were applied to both sides of the lens and the window to reduce reflection at the surface. A commercially available cooled CCD camera (BJ-42L, BITRAN) with 2048×2048 pixels installed outside of the chamber was used to measure the PSF.

To obtain a high-contrast image, we carried out the following procedure. We measured the core and the dark region, each of which have different imaging times, separately. When the dark region was measured, we obscured the light from the core with a square hole mask inserted at the first focal plane after the

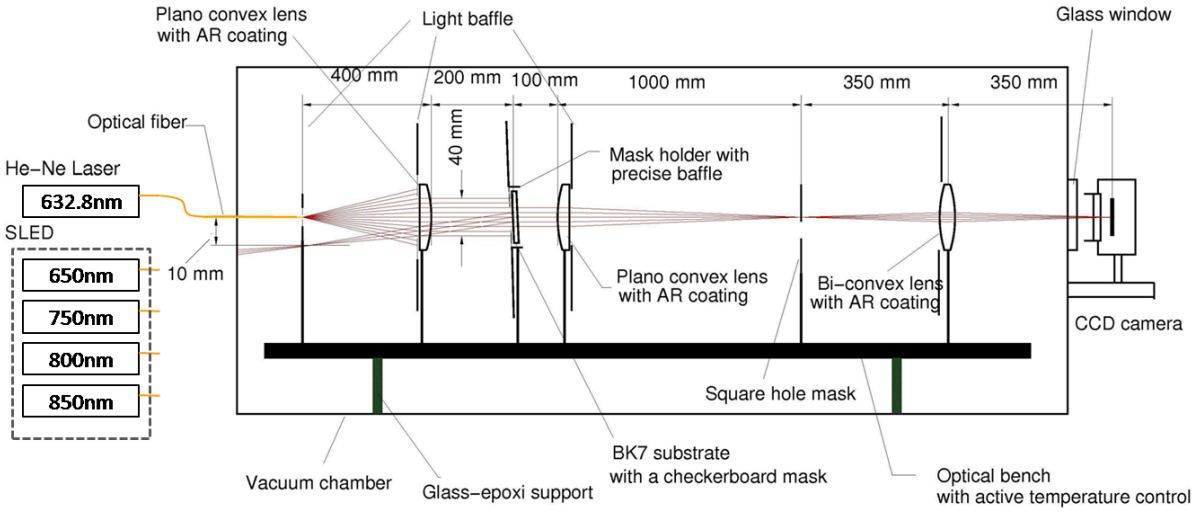

Figure 2.1: The configuration of the experimental optics.

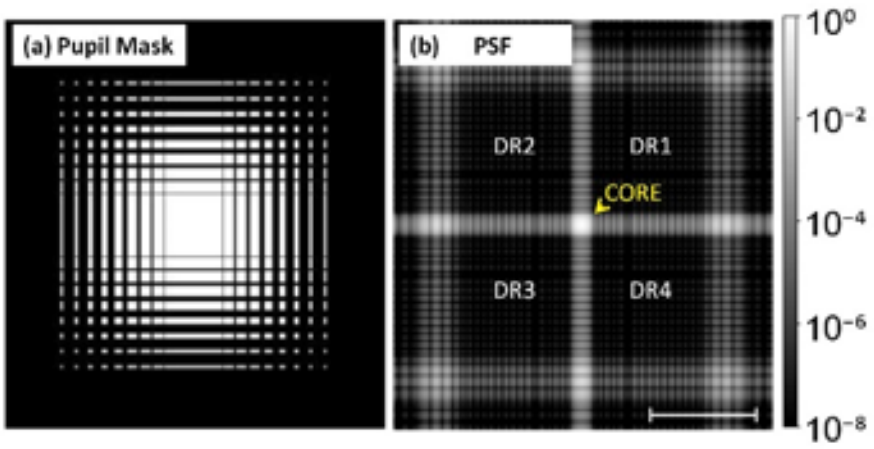

Figure 2.2: Panel (a): the pupil mask design. The transmissivity through the black and white regions is 0 and 1, respectively. The diameter of the circumscribed circle to the transmissive part is 2 mm. Panel (b): the expected (theoretical) PSF from the pupil mask. The coronagraph can make "Dark Regions (DRs)", which are areas with reduced diffracted light from the central star. There are 4 DRs near the core of the PSF. The scale bar corresponds to 20 λ /D. If a simulated planet had been present in this DR, it would have appeared as a bright spot.

pupil mask. To measure the core, we removed the square hole mask and put in two neutral density (ND) filters. The transmission through the ND filters is dependent on wavelength. We show the measurements of transmission at each wavelength in Table 2.2.

2.2 PSF subtraction experiment

2.2.1 PSF subtraction

Subtraction of the PSF is advantageous in that it removes the static WFE and achieves a higher contrast than the raw contrast of the coronagraph (Trauger & Traub, 2007). In space telescopes, the WFE caused by imperfections in the optics is an important limiting factor in the contrast of a coronagraph. PSF subtraction is available in the direct observation of exoplanets using space telescopes and helps improve high contrast observations. We demonstrated that PSF subtraction contributes to high contrast observations with a checkerboard mask in a very stable environment in the laboratory. The variations in the WFE in the laboratory experiment are attributed to thermal deformation of the optics. To maximize the effects of the PSF subtraction, it is important to improve the thermal stability of the entire coronagraphic optics.

2.2.2 Temperature stability requirement

In a previous study (Enya et al., 2007), it has been found that the contrast of the binary-shaped pupil mask coronagraph was better than 10^{-6} which is the contrast between the sun and the planets at infrared wavelengths. On the other hand, the contrast between the sun and the planets at visible wavelengths is $\sim 10^{-10}$. Among them, the contrast between the sun and the Jupiter at visible wavelengths is $\sim 10^{-9}$. We see the next step in the objectives of this study as being able to achieve a contrast of $\sim 10^{-9}$ which is the contrast required to observe giant planets directly. Therefore, we consider the temperature stability of the optical system required to achieve a contrast of $\sim 10^{-9}$ by using PSF subtraction.

In order to simplify the issue, this study focuses on the positional error in the images, which is one of the fluctuations of the images. We have arranged the data to show the relationship between the error in the position of the experimental images (ΔL [m]) and the contrast after PSF subtraction in Table2.1. The error in position of the images is assumed to be the error from the relative position of the camera and the optical system in this experimental system (Fig.2.1). For a rough estimate, we assumed that the positional error is caused by thermal deformation of the aluminum lid of the side of the HOCT chamber fastened to the camera platform and the thermal deformation of the glass epoxy plates which support the optical bench in the HOCT. First, we considered the thermal expansion of the aluminum lid. If the temperature variation is ΔT [K], the thermal expansion of the aluminum ΔL_1 [m] is

$$\Delta L_1 = L_1 \times CTE \times \Delta T, \tag{2.1}$$

Table 2.1: Contrast vs. Temperature stability

Contrast	ΔL [m]	ΔT [K]
1.9×10^{-8}	2.2×10^{-6}	0.27
9.5×10^{-9}	1.1×10^{-6}	0.14
3.8×10^{-9}	4.4×10^{-7}	0.05
1.9×10^{-9}	2.2×10^{-7}	0.02
6.3×10^{-10}	7.4×10^{-8}	0.01

where CTE=2.3×10^{-5}[K^{-1}] which is the thermal expansion coefficient for aluminum, and L_1=0.2[m] which is the length of the aluminum lid from the bottom of the chamber to the camera platform. Second, we considered the thermal expansion of the glass epoxy support. We assumed the side of the glass epoxy in contact with the chamber had a temperature variation ΔT [K] and the side of the glass epoxy in contact with the optical bench had no temperature variation because the glass epoxy is thermally insulating. Then, we assumed that the temperature variation in dL was $\frac{\Delta T}{L_2} \times L$. If the temperature variation is ΔT [K], the thermal expansion of the glass epoxy support ΔL_2 [m] is

$$\Delta L_2 = \int_0^{L_2} \frac{\Delta T}{L_2} \times L \times CTE \times dL, \tag{2.2}$$

where CTE=7.0×10^{-5}[K^{-1}], which is a typical value for the coefficient of thermal expansion for glass epoxy*, and L_2=0.1[m], which is the length of the glass-epoxy support. We considered a simplified case in which the thermal deformation of the aluminum and the thermal deformation of the glass epoxy plates give the error in the position of the images,

$$\Delta L = \Delta L_1 + \Delta L_2, \tag{2.3}$$

Then we show the data giving the relationship between the error in position of the images (ΔL [m]) and the temperature variation (ΔT [K]) in Table 2.1. As shown in Table 2.1, the temperature variation ΔT has to be ∼0.01K in order to aim for a contrast of $\sim10^{-9}$.

2.2.3 Stable environment in HOCT

To reduce the instability caused by air turbulence and thermal instability, the coronagraphic optics were installed on an optical bench set in a vacuum chamber. The optical bench was set on supports consisting of glass epoxy plates to prevent thermal conduction from the chamber. To reduce the thermal instability, active PID temperature control was applied to the optical bench using a silicon diode temperature sensor and three resistance heaters. These are

*http://www.hitachi-chem.co.jp/english/products/bm/b01/001.html

described in our previous study (Haze et al., 2009). In this study, we added new functions to the experimental system as follows. We used multi-layer insulation (MLI), consisting of an aluminum film on a polyethylene foam mattress, on the windows in the experiment room to reduce radiation from the windows. In addition, we controlled the room temperature with an air conditioner and installed fans to obtain thermal equilibrium through convection. To reduce thermal deformation, the whole external surface of the vacuum chamber was covered with eight sheets of MLI. We monitored the change of temperature on the surface of the vacuum chamber and the camera stage using a total of eight silicon diode temperature sensors (DT-670A1-SD, LakeShore) and a temperature monitor (Model 218, LakeShore). Before introducing the MLI, a cyclical change in temperature with a period of about 1000sec was observed in all eight channels and the temperature variation range was about 0.1K (peak-to-peak). After introducing the MLI, this cyclical change in temperature was not observed in any of the channels and the temperature variation range in every channel was significantly reduced to less than 0.03K (peak-to-peak). Consequently, we were able to ascertain whether the thermal stability had an effect on the PSF subtraction in our experiments.

We used Mask2 developed in Enya et al. (2007). The mask is a checkerboard mask, which is a type of binary-shaped pupil mask (Vanderbei et al., 2004). Fig.2.2 shows the design. The central brightest region of the PSF is called the "core", and the four regions near to the core, in which diffracted light is reduced, is called the "dark region". The contrast, inner working angle (IWA), and outer working angle (OWA) are 10^{-7} , $3\lambda/D$, and $30\lambda/D$, respectively, where λ is wavelength and D is the diagonal of the checkerboard mask. Optimization of the mask shape was performed using the LOQO solver presented by Vanderbei (1999). The pupil mask consists of a 100nm thick aluminum film on a BK7 substrate, and was manufactured using nano-fabrication technology at the National Institute of Advanced Industrial Science and Technology (AIST) in Japan. A standard BMAR coating optimized for use at a wavelength of 632.8nm was applied to both sides of the substrate.

2.2.4 Core image

We used a He-Ne laser in this experiment. The core images of the coronagraphic PSF were taken with a combination of several exposure times (0.03, 0.3, 3, 10s). The CCD was cooled and stabilized at $271.0 \pm 0.5K(1\sigma)$. We inserted two ND filters as previously mentioned. After each imaging process, the laser source was turned off and a "dark frame" measurement was taken with the same exposure time and the same optical density filter. The dark frame was subtracted from the image with the laser light on and we obtained a "raw" coronagraphic image (Fig.2.3a). This result is quite consistent with that expected from theory, as shown in Fig.2.2b.

2.2.5 Raw image of dark region

The dark region of the coronagraphic image was observed with a 200s exposure. A "dark frame" was taken with a 200s exposure and this was then subtracted from the dark region image with the laser light on. The CCD was at the same temperature as when the core images were observed. The observed dark region of the raw coronagraphic image is shown in Fig.2.3b. The "Lattice pattern" consisting of dots in the "raw" dark region corresponds to the diffraction pattern caused by the checkerboard mask and hence it is limited by the design of the mask. In other words, the current experimental contrast approximately reached the design value. We evaluated the contrast between the areal mean of the observed dark region and the peak of the core. The observed dark region is the area of the image through the square hole mask. As a result, a raw contrast of 2.3×10^{-7} was obtained.

2.2.6 PSF subtracted image of dark region

To obtain a contrast better than the design limit, we introduced PSF subtraction. The dark region of the coronagraphic image was observed twice in sets of $200s \times 18$ exposures (3600s). 18 frames in each set of dark regions were combined and as a result two images totaling 3600s exposure were obtained. We obtained the dark region as a result of PSF subtraction using these two images. The images after PSF subtraction are shown in Fig.2.3 (c). There are some residual patterns on the dark region compared to the background as shown in Fig.2.3 (c). The dark region consists of a "lattice pattern" derived from the design of the mask, "speckle" from systematic errors in the experiment and "random noise" including dark current and readout noise. The background consists of random noise. Thus, the residuals on the dark region after PSF subtraction are composed of the residual background noise and the residual coronagraphic image (lattice pattern and speckle). Hence, the upper limit of the contrast is 5.3×10^{-9} defined as the ratio between the standard deviation of the subtracted dark region ($1\sigma_{DR}$) and the peak of the core. It is necessary to factor out the residual background noise in order to estimate the residual coronagraphic image. The standard deviation (1σ) of the coronagraphic image after PSF subtraction, is defined by $\sigma = \sqrt{\sigma_{DR}^2 - \sigma_{BG}^2}$, where σ_{DR} is the standard deviation of the dark region and σ_{BG} is the standard deviation of the background (Fig.2.4). We evaluated the contrast between the σ after PSF subtraction and the peak of the core. A contrast of 1.3×10^{-9} was achieved for the PSF subtracted image. If a brighter light source is used, this contrast could, in principal, become feasible.

Fig.2.5 shows one dimensional profiles of the coronagraphic images obtained by measurement. Scaling by the exposure time and the optical density allowed smooth profiles of the core to be obtained.

We considered a detection threshold in order to carry out a practical comparison of the contrast before and after the PSF subtraction. After PSF subtraction, the contrast was estimated using the standard deviation of the dark region, as adopted in Biller et al. (2009). As shown in Fig.2.4, a Gaussian dis-

tribution was confirmed by plotting values of the dark region and 1σ covering $\sim 70\%$ of the dark region. Before PSF subtraction, the contrast was estimated using the areal mean of the dark region. We checked the values of the observed dark region and confirmed that the areal mean also covered $\sim 70\%$ of the dark region. Therefore, we estimated that the contrast was improved by almost two orders of magnitude when compared with the raw PSF. In other words, this shows that the adiabatic vacuum chamber was successful in reducing the instabilities caused by thermal deformation of the optics reported previously Haze et al. (2009). It should be noted that the result demonstrates the stability of our apparatus. The stability and an understanding of it are expected to be valuable in more complex future experimental environments with the chamber.

2.3 Multi-color/broadband experiment with SLED

For an actual observation, it is necessary to observe over a wavelength band and it is beneficial to observe multiple bands. In principle, the binary-shaped pupil mask coronagraph can make observations over a wide range of wavelengths. To demonstrate this, we used Mask 2 and the light source was changed from a He-Ne laser to broadband and multi-band light sources. Super luminescent Light Emitting Diodes (SLEDs) from EXALOS were used as multi-band and broadband light sources at four wavelengths (center wavelengths of 650nm, 750nm, 800nm and 850nm). The wavelengths and bandwidths are presented in Table 2.2. The CCD was cooled and stabilized at $271.0 \pm 0.5K(1\sigma)$. The temperature of the CCD could not be reduced to the temperature used for the PSF subtraction experiment and we assume that this was because of a functional problem in the CCD cooler. The wavelength was changed by connecting the optical fiber outside the chamber to each light source in turn. For each of the four wavelengths, the core and dark region images were observed without reconnecting the light source in order to prevent changes in intensity.

The resulting images are shown in Fig.2.6. The core images were taken with several exposure times (0.3, 0.6, 0.9, 1.2, 12, 24s) and the dark region images were taken with 120s and 300s exposures. As mentioned previously, we inserted two ND filters when we took the core images. A "dark frame" was then subtracted from the image with the SLED light on. We evaluated the contrast between the areal mean of the observed dark region and the peak of the core. As a result, we achieved contrasts of 3.1×10^{-7}, 1.1×10^{-6}, 1.6×10^{-6} and 2.5×10^{-6} at 650nm, 750nm, 800nm and 850nm, respectively (Fig.2.5).

The results show that the contrast was significantly improved compared with non-coronagraphic optics within each of the wavelength bands. We also found the contrast degrades as the wavelength gets longer and a ghost image was observed at longer wavelengths (Figs.2.6 b,d,f,h). Our suggestions on these issues are as follows.

1. Wavelength dependency of the focal position : In this experiment, we

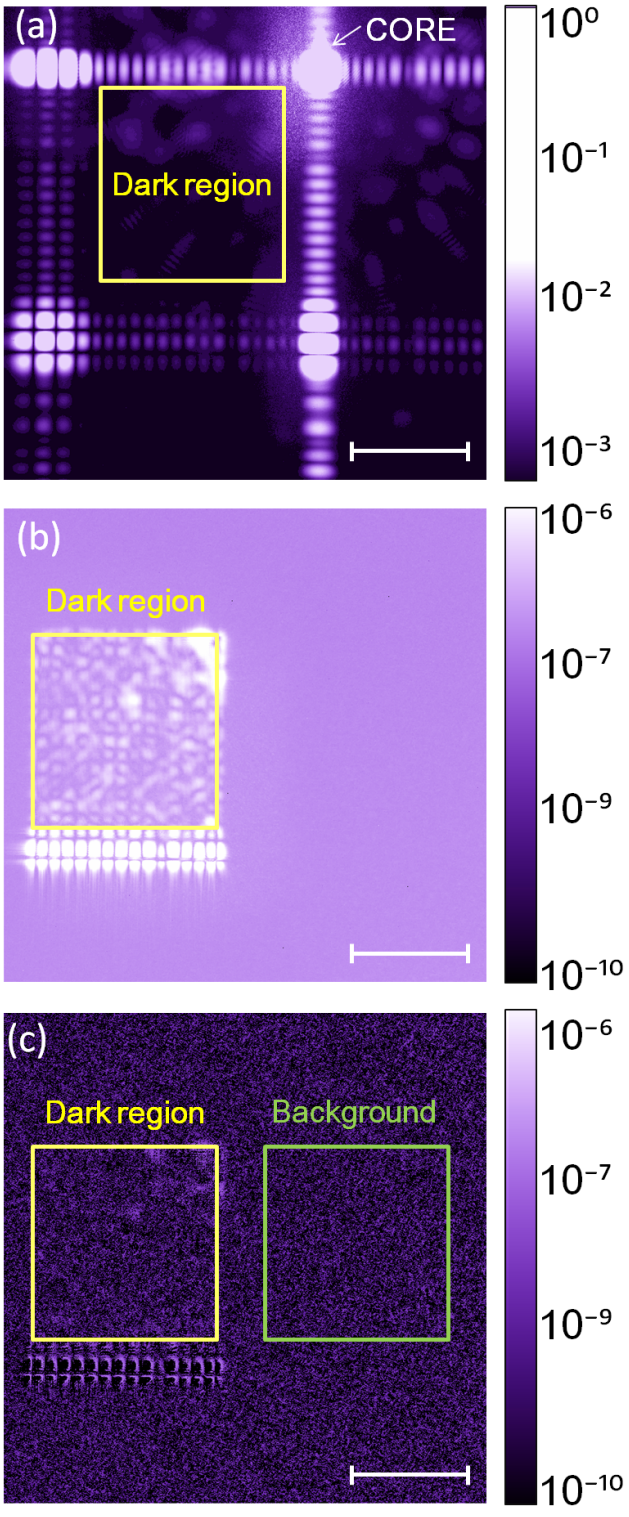

Figure 2.3: Observed coronagraphic images obtained with a He-Ne laser. Panel (a): an image including the core of the PSF obtained with the ND filters. Panel (b): a raw image of the dark region (the yellow rectangle) obtained with the square hole mask. Panel (c): an image of the result of PSF subtraction using two raw coronagraphic images. The green rectangle shows the area used to derive the background level in the analysis. The scale bars correspond to $10\lambda/D$.

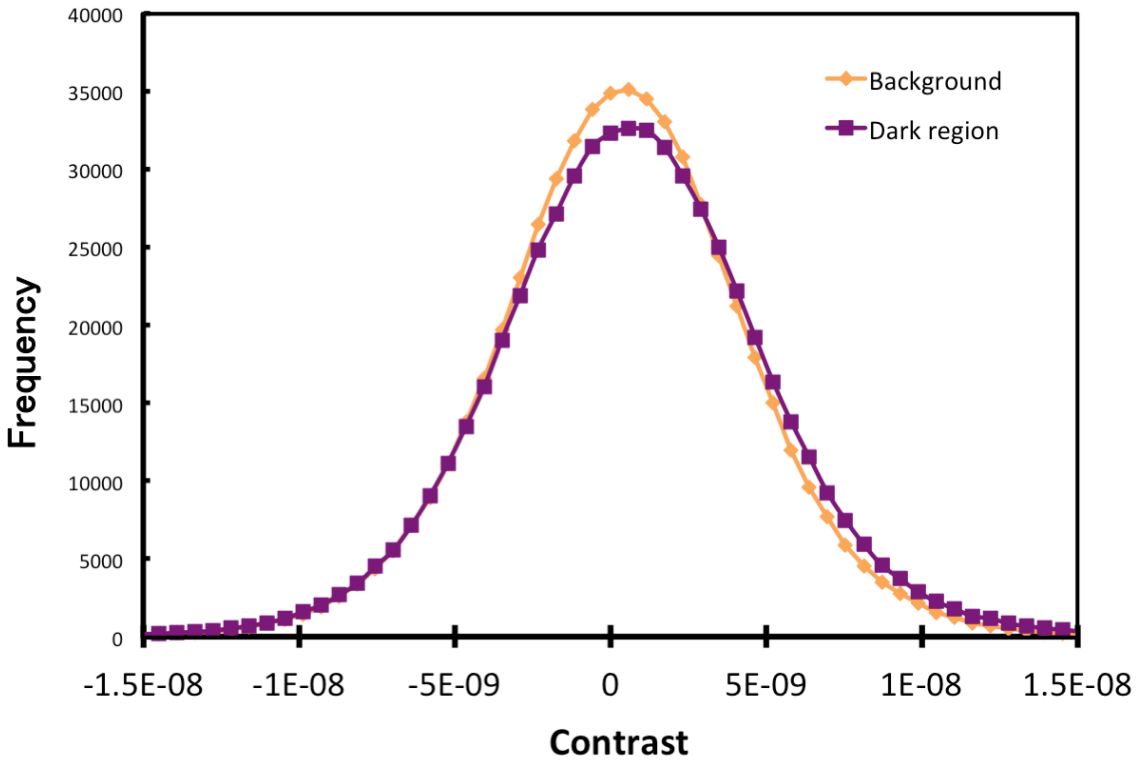

Figure 2.4: Histograms of the dark region and the background. The values of the dark region and the background normalized by the peak intensity of the core are plotted on the x axis and their frequencies are on the y axis. A Gaussian distribution was confirmed by plotting the values of the dark region and the background.

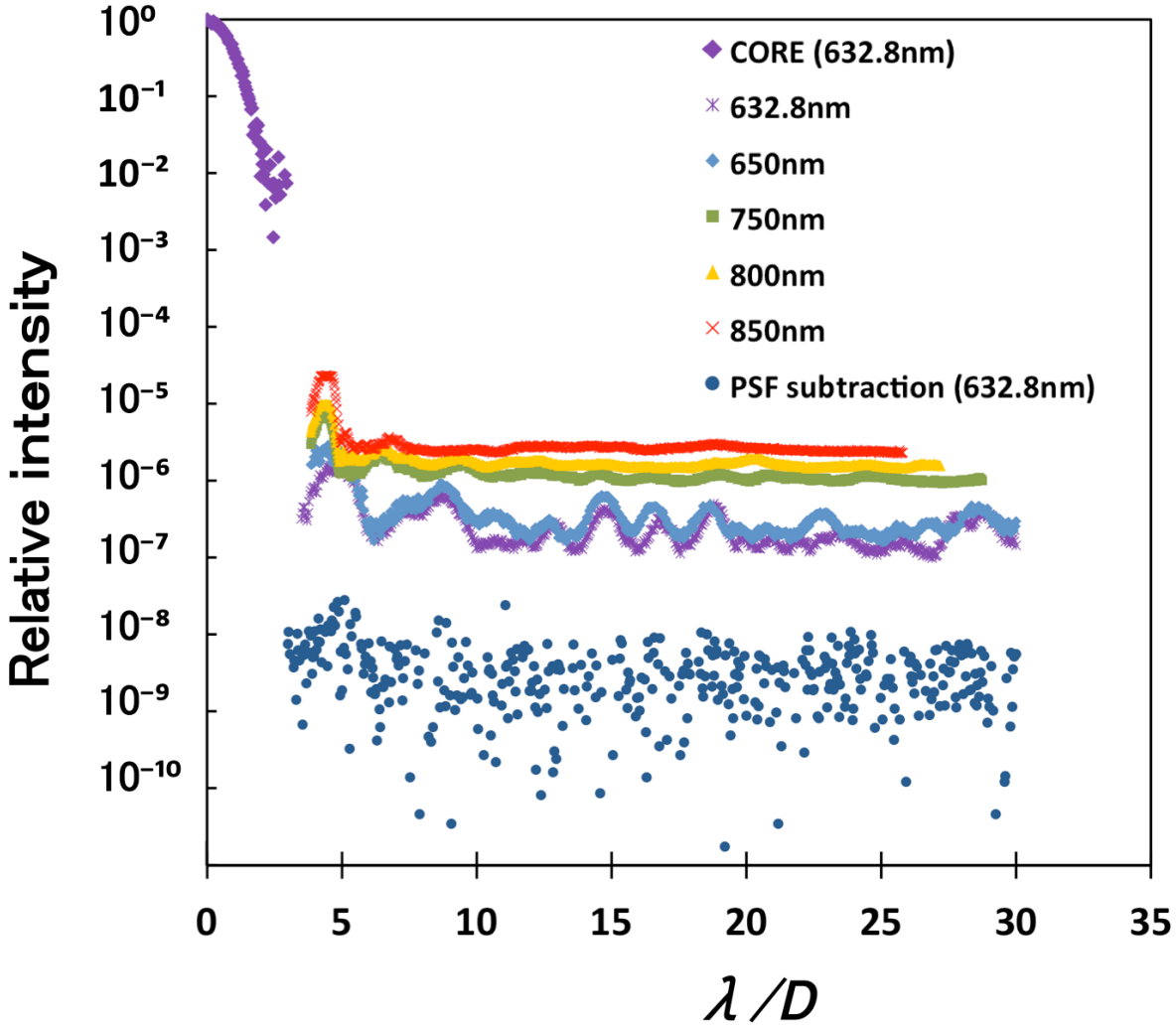

Figure 2.5: Diagonal profiles of the observed coronagraphic PSF. Each profile is normalized by the peak intensity.

Table 2.2: Property of light sources and ND filters.

Light source	λ_c [nm]	$\Delta\lambda$ [nm]	ND transmissivity [%]
He-Ne laser	632.8	-	0.0088
SLED	650	8	0.016
SLED	750	21	0.25
SLED	800	25	0.30
SLED	850	55	0.32

$*$ Total transmission through the two ND filters at λ_c.

changed each wavelength by reconnecting the optical fiber outside the chamber without changing the configuration of the optical system inside the chamber, which had been adjusted for the He-Ne laser. The focal planes at the various wavelengths did not coincide because the lenses have different refractive indices for different wavelengths of light. Therefore, we checked whether a major cause of the deterioration in contrast was due to reducing the peak of the core by defocusing. As a result of simple ray trace analysis with ZMAX software, the difference in focal plane position in the entire optical system was up to 60.6mm and the contrast at 850nm was worse than the contrast at 632.8nm by a factor of only 1.32. Thus, this was not a major cause of degradation in the contrast.

2. Wavelength dependency of the residual reflectance of the BMAR coating : The lenses we used have BMAR coatings. The residual reflectance of the lens has a wavelength dependence, as shown in Fig.2.7. The BMAR coatings do not work so well at longer wavelengths. Ghost images may have appeared and the brightness in the dark region may have increased because of the increase in reflected light. In principle, this problem can be solved by replacing the lens with mirrors. Therefore, we are preparing a mirror optics system, which requires drastic changes to replace the one-dimensional optical bench with a two-dimensional testbed.

We checked whether a contrast of 10^{-7} was achieved for the relatively-clean dark region. As shown in Figs.2.8 (a), (b), (c) and (d), the areal mean of part of the dark region (green square) was calculated. We obtained contrasts of 2.7×10^{-7}, 9.2×10^{-7}, 1.4×10^{-6} and 2.2×10^{-6} at 650nm, 750nm, 800nm and 850nm, respectively. It was found that there were structured ghosts (in Fig.2.8, see orange circles) and the ghosts were spread across the dark region.

We also checked whether the ghosts were removed by PSF subtraction. We subtracted the images taken with 300s exposures at the same wavelength, as shown in Figs.2.8 (e), (f), (g) and (h). We evaluated the contrast between the standard deviation of the subtracted dark region and the peak of the core. As a

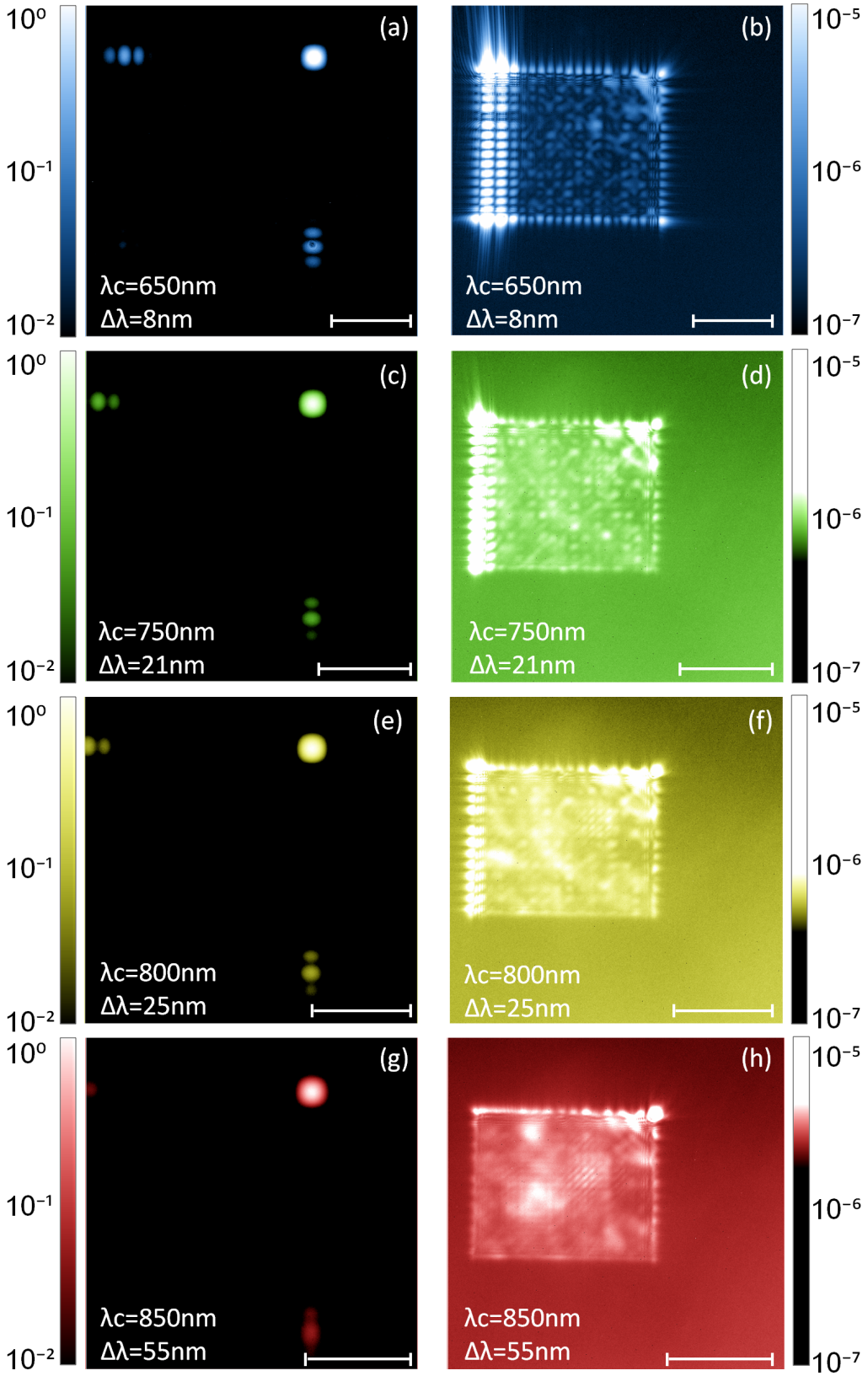

Figure 2.6: Observed coronagraphic images obtained with SLEDs. Panels (a), (c), (e), and (g) show images including the core of the PSF obtained with the ND filters, and panels (b), (d), (f) and (h) show images of the dark regions obtained with the square hole mask, respectively. The scale bars corresponds to $10\lambda/D$.

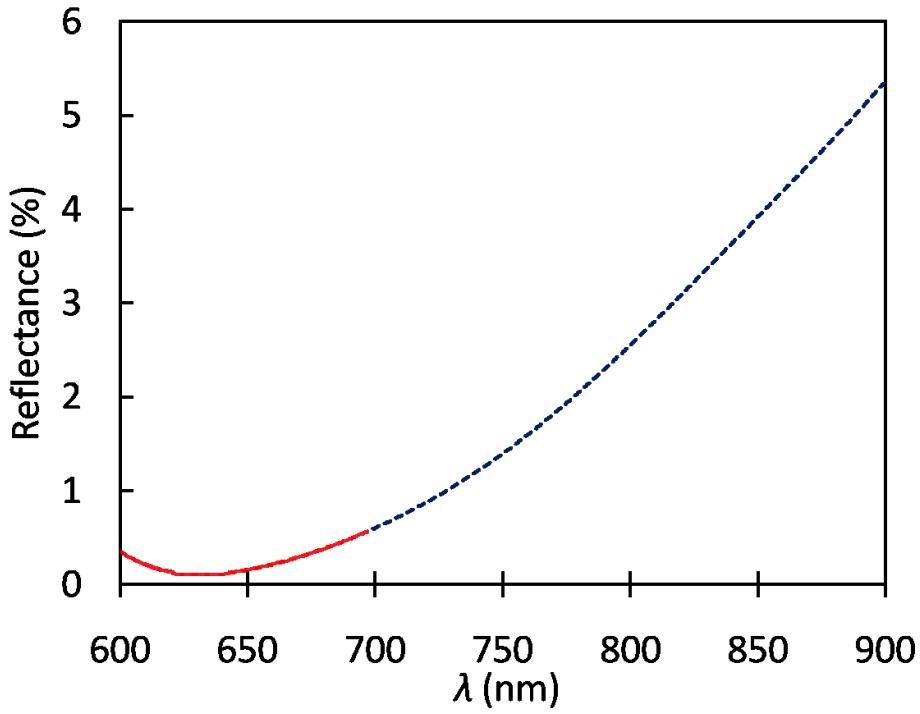

Figure 2.7: Residual reflectance of BMAR coating. The solid red and dashed blue lines are plots based on the experimental and theoretical values, respectively.

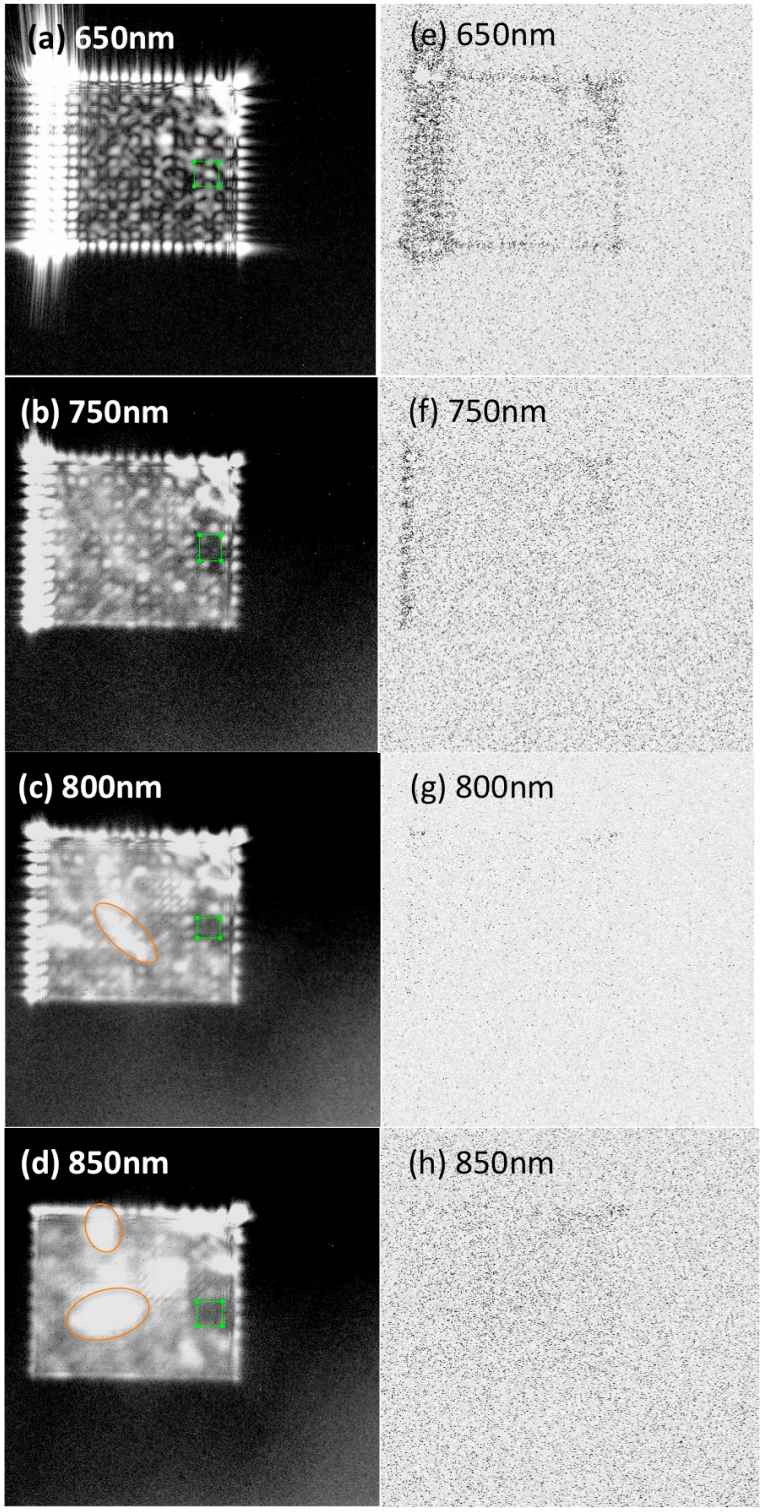

Figure 2.8: Panels (a), (b), (c), and (d) show images of the dark regions, respectively. The green square regions are chosen as the relatively-clean dark regions. Panels (e), (f), (g) and (h) show images of the dark regions after the PSF subtraction.

result, we obtained contrasts of 2.0×10^{-8}, 3.7×10^{-8}, 2.6×10^{-8} and 7.2×10^{-8} at 650nm, 750nm, 800nm and 850nm, respectively. It was found that the ghosts were removed by PSF subtraction and the contrasts were improved.

2.4 Free-standing pupil mask experiments

In the previous section, we demonstrated the basic properties of binary-shaped pupil mask coronagraphs. However, a glass substrate mask, which has been successfully used in previous experiments with visible light, has the following problems; the substrate suffers from transmission losses, ghosting from residual reflectance occurs, and the refractive index depends on the wavelength.

On the other hand, a free-standing mask has the advantages of no transmission losses, no ghosting from residual reflectance and a refractive index that is independent of wavelength. Therefore, we have developed a new free-standing mask made from sheet metal without the use of a substrate. We conducted free-standing mask coronagraph experiments with the HOCT and evaluated the contrast performance of the free-standing mask. Details are discussed in the following section.

2.4.1 New free-standing pupil mask

In this section, we describe the design and performance of the new free-standing mask (Fig.2.9). The mask is a checkerboard mask (Fig.2.10(a)). There are four dark regions near to the core of the PSF, as shown in Fig.2.10(b). The designed contrast, IWA, and OWA are 10^{-10} , $5.4\lambda/D$, and $50\lambda/D$, respectively. The free-standing mask, formed of copper laminate, was fabricated with high-accuracy electroforming. We increased the pupil-mask size to 10mm from 2mm because of the difficulty in making 2mm size free-standing masks.

A photomask with the pattern was made first, and then the free-standing mask was made by photolithography using the photomask. The manufacturing processes of the photomask and the free-standing mask are described in the Appendix.

2.4.2 Optical system

The optical system in the HOCT is shown in Fig.2.11. The light source is a He-Ne laser as in the PSF subtraction experiment in Section 2.2. The distinctive configuration of this experiment is as follows. We used a free-standing mask, 10mm in size, designed to give a contrast of 10^{-10}. The mask is larger than Mask 2, which is 2mm in size. A CCD camera was set up in the chamber. We used 3.4× relay optics after the focal plane mask with the change of mask size and camera position.

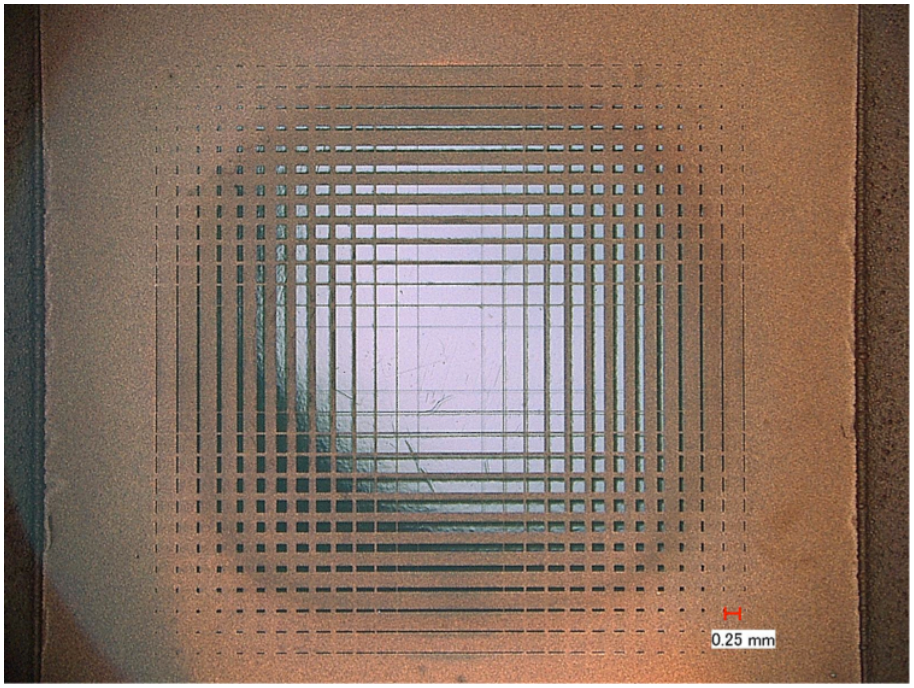

Figure 2.9: The new free-standing mask formed of copper laminate. The transmissive region is 10mm on a side.

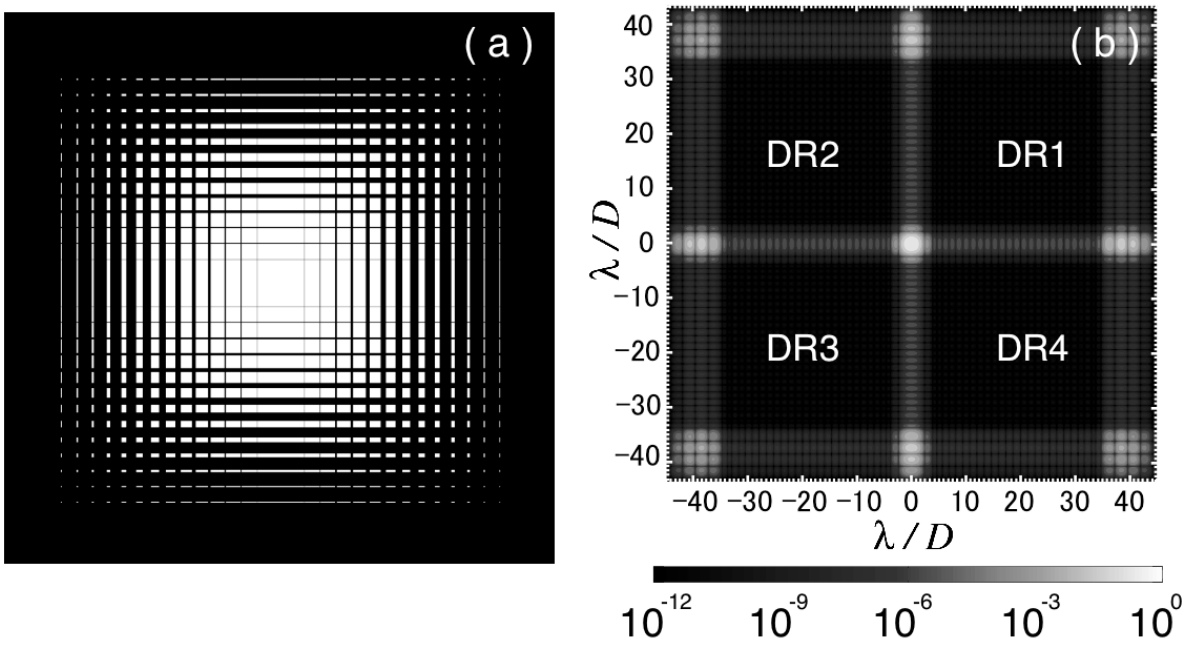

Figure 2.10: Panel (a) Design of the free-standing mask. The transmissivities of the black and white regions are 0 and 1, respectively. Panel (b) Simulated coronagraphic PSF, using the mask design shown in panel (a).

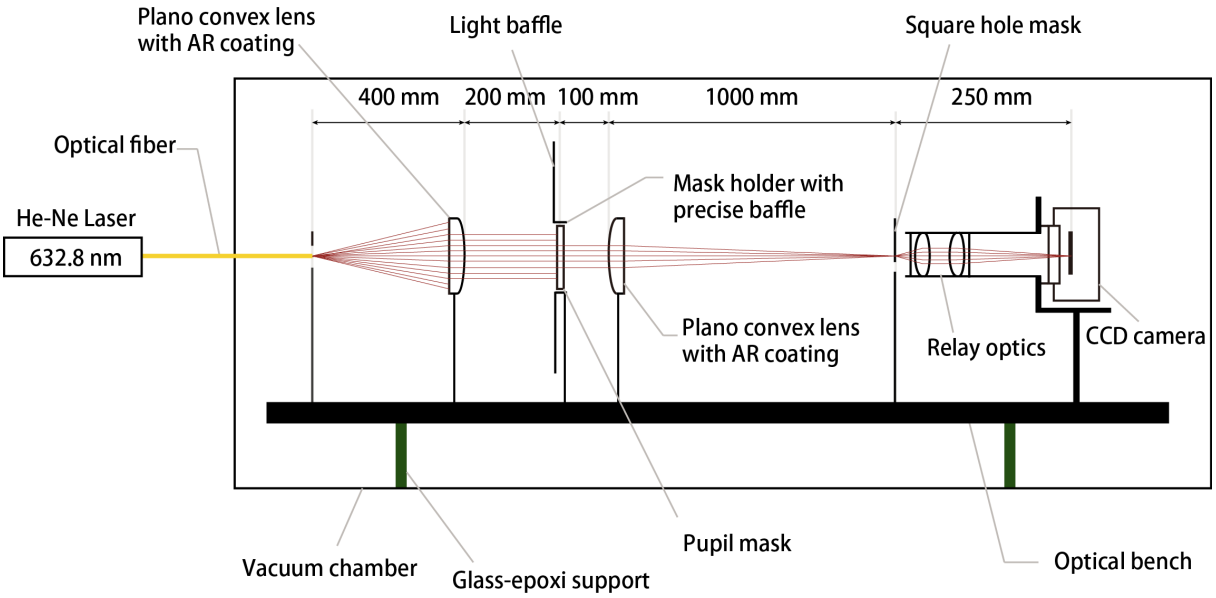

Figure 2.11: The configuration of the experimental optics.

2.4.3 Imaging procedure

To obtain a high-contrast image, we measured the core and the dark region separately, since each have different exposure times,.

The core images of the coronagraphic PSF were taken with a combination of several sets of exposure times (0.3, 3, 10s) using two ND filters. After each imaging process, the laser source was turned off and a "dark frame" measurement was taken with the same exposure time and the same ND filters. The dark frame was subtracted from the image with the laser light on and we obtained a "raw" coronagraphic image (Fig.2.12(a)).

The dark region of the coronagraphic image was observed with 300s exposure using a square hole focal-plane mask. We took four images (DR1 - DR4) shifting the focal-plane mask, where DR1 - DR4 are the dark regions corresponding to the quadrants around the core shown in Fig.2.10(b). A "dark frame" was taken with 300s exposure and this was then subtracted from the dark region image with the laser light on. The observed dark regions of the raw coronagraphic image are shown in Fig.2.12(b)(c)(d)(e).

2.4.4 Contrast of the free-standing mask

Observed coronagraphic images are shown in Fig.2.12. Fig.2.13 shows diagonal profiles of the observed coronagraphic PSF, the designed coronagraphic PSF and the Airy PSF.

The images and profiles of the core of the observed coronagraphic PSF are quite consistent with those expected from theory. The relative intensity over most of the area of the dark region was less than 10^{-6}, as shown in Fig.2.13 . We evaluated the contrast between the areal mean of the observed dark

region and the peak of the core. The contrast values are 9.6×10^{-8}, 9.6×10^{-8}, 9.5×10^{-8} and 1.2×10^{-7} for DR1, DR 2, DR 3 and DR4, respectively. The average contrast for all the dark regions is 1.0×10^{-7}. Figure2.12(b)(c)(d)(e) also exhibits irregular speckles in the dark regions, which are not predicted by the theoretical PSF for the mask.

2.4.5 Rotated mask subtraction

The results of free-standing mask experiments have demonstrated that the contrast was 1.0×10^{-7}, while the designed contrast is 10^{-10}. Speckles are the major limiting factor. We suppose that the major factors causing the speckles are (1) pupil-mask shape error and (2) other errors in the optical-system except the mask.

We consider that the method of rotating only the pupil-mask of the coronagraphic optics will work to separate the mask shape error and the other errors, because we expect that speckles from the mask shape error rotate with the mask.

First, we subtracted the images without mask rotation for confirmation of the stability of the optical system. We evaluated the contrast between the standard deviation of the subtracted dark region and the peak of the core. As a result, a contrast of 8.1×10^{-8} was obtained. The result shows that the contrast was significantly improving compared with the raw contrast. Therefore, it is worth trying to evaluate the improvement attained by rotated mask subtraction using the optical system. Thus, we rotated the mask 90 degrees around the central axis perpendicular to the mask surface to confirm whether the intensity distribution of the irregular speckle pattern changed. After that, we subtracted the image after mask rotation (Fig.2.14) from the image before mask rotation (Fig.2.12). Rotated mask subtraction can be done in two different ways (Rotated mask subtraction 1 and 2).

1. Rotated mask subtraction 1 is where the image is rotated -90 degrees after mask rotation and subtracted from the image before mask rotation. In other words, this is a way of subtracting speckles in the dark regions associated with the direction of the mask. If the speckles are only due to mask shape errors, rotated mask subtraction1 is expected to improve the contrast. This is because speckles in the dark regions are associated with the direction of the mask in this case. We rotated the images -90 degrees after mask rotation. We shifted the core image before mask rotation to fit the center of the core before and after mask rotation, and then the shift was applied to the dark region images. We increased the intensity of the dark region before mask rotation by 1.27 times to be consistent with both the areal mean of the dark regions before and after mask rotation. We subtracted the images after adjusting the position of the PSF and the intensity as above. There are four ways to carry

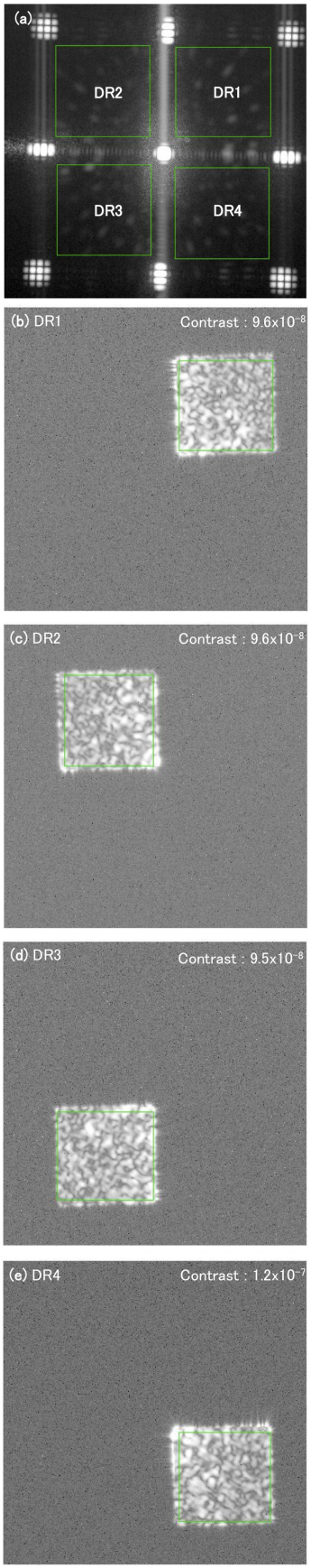

Figure 2.12: Observed coronagraphic images before mask rotation. Panel (a): an image including the core of the PSF. Panels (b), (c), (d) and (e): raw images of the dark regions. The areal means in each green rectangle in DR1 - 4 were obtained.

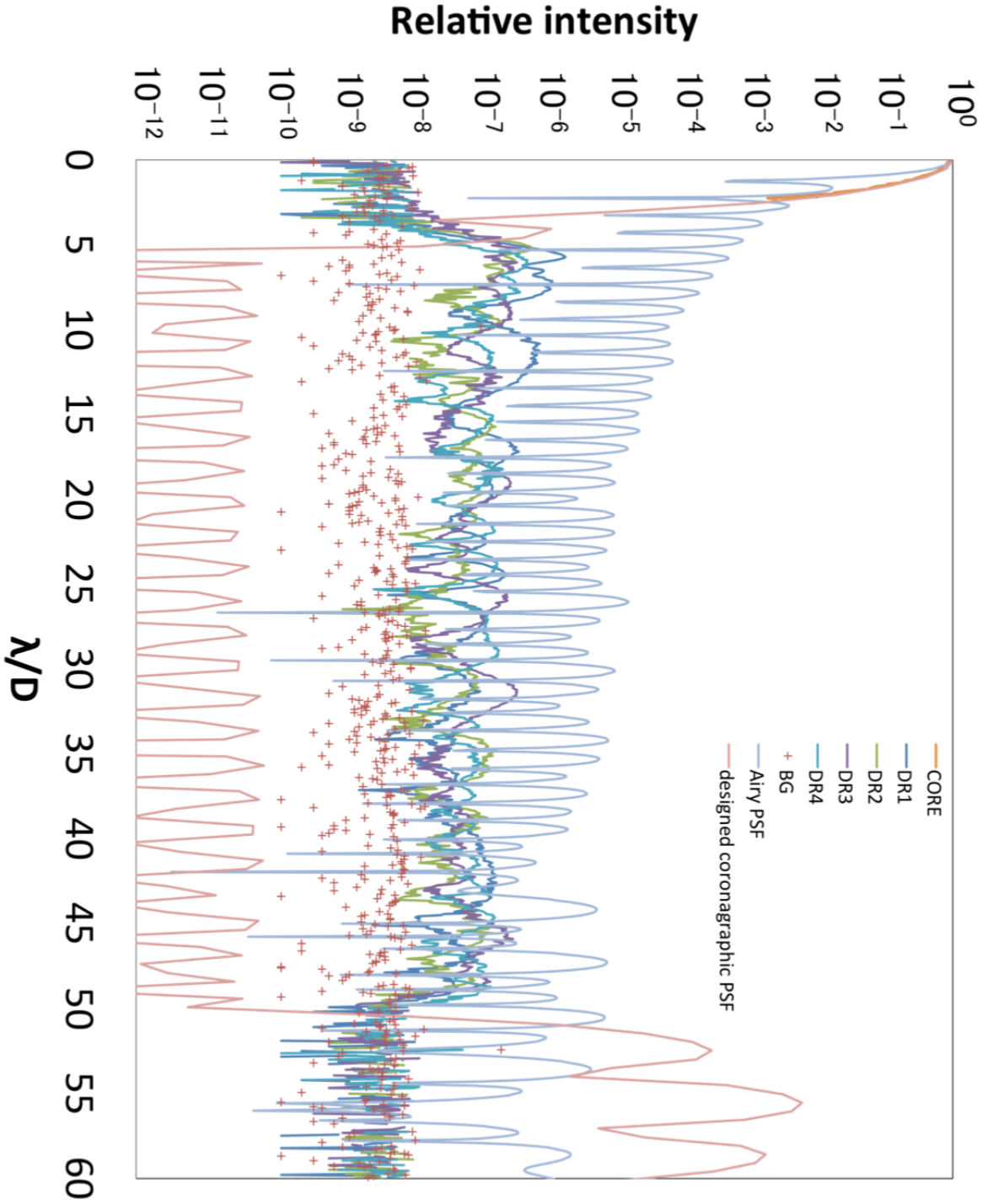

Figure 2.13: Diagonal profiles of the observed coronagraphic PSF, designed coronagraphic PSF and Airy PSF. Each profile is normalized by the peak intensity.

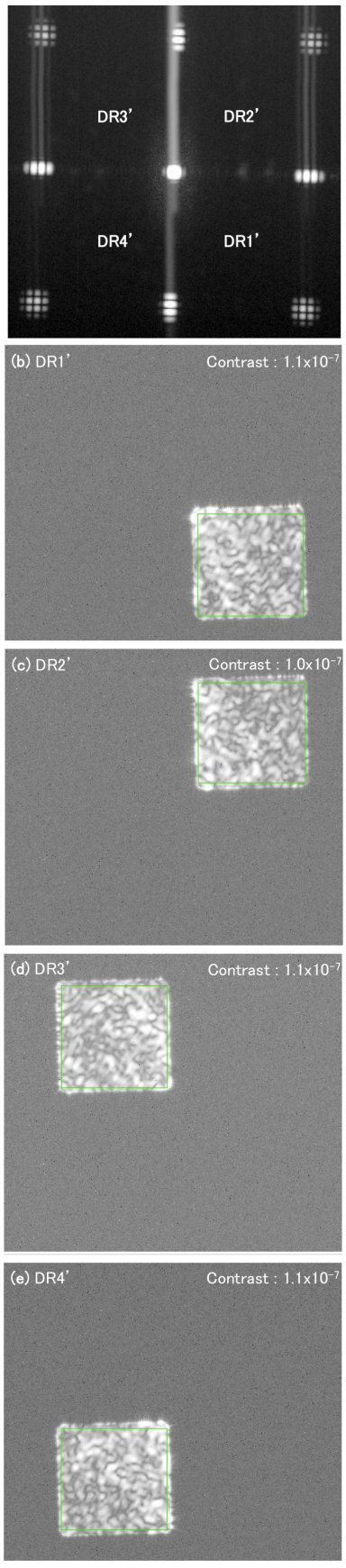

Figure 2.14: Observed coronagraphic images after mask rotation. Panel (a): an image including the core of the PSF. Panels (b), (c), (d) and (e): raw images of the dark regions. The areal means of each green rectangle in DR1 ' - 4 ' were obtained.

out the subtraction (DR1-DR1', DR2-DR2', DR3-DR3', DR4-DR4'). Fig.2.15 shows the PSF after rotated mask subtraction 1. Comparing the speckle patterns before and after mask rotation, the speckle patterns are completely different, as shown in Fig2.12, 2.14. Also, the residuals on the rotated mask subtraction image, as shown in Fig2.15, are different from the residuals from misalignment of the images. Therefore, the residuals from misalignment of the images are not the main components of the residuals in the subtracted image. We evaluated the contrast between the standard deviation of the dark region after rotated mask subtraction 1 and the peak of the core. The approach used to estimate the contrast using the standard deviation of the dark region, as adopted in Biller et al. (2009). As a result, contrasts of 1.3×10^{-7}, 1.4×10^{-7}, 1.3×10^{-7} and 1.5×10^{-7} at DR1 - DR1', DR2 - DR2', DR3 - DR3' and DR4 - DR4' were achieved for the images from rotated mask subtraction 1. The contrasts showed no improvement compared with the contrasts before subtraction. In other words, this means the speckles are not due to mask shape errors only, but are also due to errors in the optical-system. We consider that the errors in the optical-system consist of WFEs, non-uniform intensity, stray light and so on.

2. Rotated mask subtraction 2 is where the image after mask rotation are subtracted from the image before mask rotation. If the mask shape and repeatability of the mask position are perfect, rotated mask subtraction 2 is expected to improve the contrast. This is because the errors in the optical-system, such as WFEs are common to images both before and after mask rotation. We shifted the core image before mask rotation to fit the centers of the core before and after mask rotation, and then the shift amount was applied to the dark region images. We increased the intensity of the dark region before mask rotation by 1.27 times to be consistent with both the areal mean of the dark regions before and after mask rotation. We subtracted the images after adjusting the position of the PSF and the intensity as above. There are four ways to carry out the subtraction (DR1-DR2', DR2-DR3', DR3-DR4', DR4-DR1'). Fig.2.16 shows the PSF after rotated mask subtraction 2. We evaluated the contrast between the standard deviation of the dark region after rotated mask subtraction 2 and the peak of the core. As a result, contrasts of 1.2×10^{-7}, 1.7×10^{-7}, 1.7×10^{-7}, 1.4×10^{-7} at DR1 - DR2', DR2 - DR3', DR3 - DR4', DR4 - DR1' were achieved for the images from rotated mask subtraction 2. No improvement in the contrasts was found compared with the contrasts before subtraction. These results show the mask shape and/or the repeatability of the mask position are not perfect.

These results of rotated mask subtraction show the speckle is not due to the mask shape error alone. The speckles arise because of errors in the optical-system also. The speckles are due to errors in the optical-system (e.g., the WFE, non-uniform intensity and stray light) or the combined effect of the mask shape error and errors in the optical-system except the mask. A useful

way of distinguishing between the mask shape errors, errors in the optical-system and the error in replicating the mask position is to simulate the effects of these errors.

2.4.6 Numerical simulations of some mask shape errors

We simulated the PSFs with only a mask shape error. We considered a simplified case of an across-the-board increase in the line width of the mask pattern where the light is blocked. Fig.2.17 shows simulated PSFs from across-the-board 5, 10, 15, 20μm increases in the line width of the free-standing mask. In the case of an across-the-board 20μm increase in line width, the smallest holes, where light passes through the mask, are closed. When we checked the holes of the free-standing mask using a digital microscope (VHX-900, KEYENCE), we found holes in the positions expected from the mask design. Thus, the case of an across-the-board 20μm increase is worse than achieved in reality and is an extreme case. So, we ignored the case of an across-the-board increase of more than 20μm. Even in the case of an across-the-board 20μm increase in line width, the contrast in the dark region was not worse than 10^{-7}. Therefore, this suggests that the speckle was not due to mask shape errors alone. This result of the numerical simulations of the mask shape errors is consistent with the result of Rotated mask subtraction 1.

2.4.7 Numerical simulations of WFEs

In this section, we show the results of the simulation of the PSFs without a mask shape error, but with only a wavefront error. First of all, we simulated the PSF that reproduces the experimental raw contrast ($\sim 10^{-7}$) by using the appropriate wavefront error. One of the preferred metrics used for specifying wavefront errors is the power spectral density (PSD). It is computed from the amplitudes of the spatial frequency components present in the Fourier spectrum of the surface height of pupil-plane. In reference to Sidick (2009), we used the following Lorentzian equation as our PSD function:

$$PSD = \frac{\sigma_0^2 A}{h_0} \frac{1}{1 + (\rho_{mn}/\rho_{HP})^p}, \tag{2.4}$$

where σ_0 is the rms value, A is the mask size, ρ_{mn} is the spatial frequency (m^{-1}), ρ_{HP} is the half-power frequency (m^{-1}), p is a power law, and $h_0 = \sum_{m=1}^{M} \sum_{n=1}^{N} \frac{1}{1+(\rho_{mn}/\rho_{HP})^p}$.
We chose $\rho_{HP} = 4.3$ m^{-1} with reference to the HST mirror (Borde & Traub, 2006). Substituting certain values for σ_0 and p, we simulated the PSFs. We chose the best fit which minimizes the sum of the squared residuals, a residual being the difference between an observed radial average and the simulated radial average, as shown in Fig.2.18. In this simulation, the RMS from the wavefront error is 3.5 nm ($\lambda_0/180$), where $\lambda_0 = 632.8$ nm.

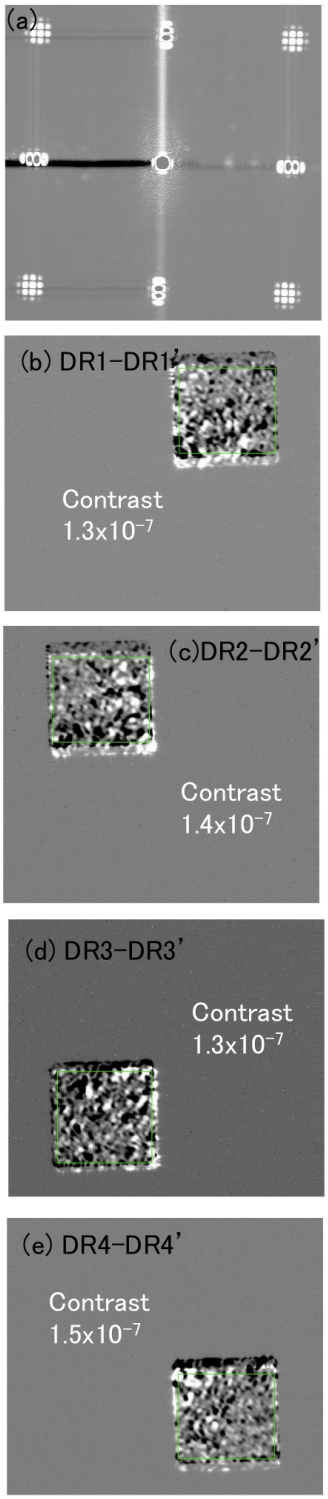

Figure 2.15: Rotated mask subtraction 1: the way in which the image was rotated by -90 degrees after mask rotation and subtracted from the image before mask rotation. Panel (a): shifting the core image before mask rotation to fit the centers of the cores before and after mask rotation. Panels (b), (c), (d) and (e): images of the results of rotated mask subtraction 1 (DR1-DR1 ' , DR2-DR2 ' , DR3-DR3 ' , DR4-DR4 ').

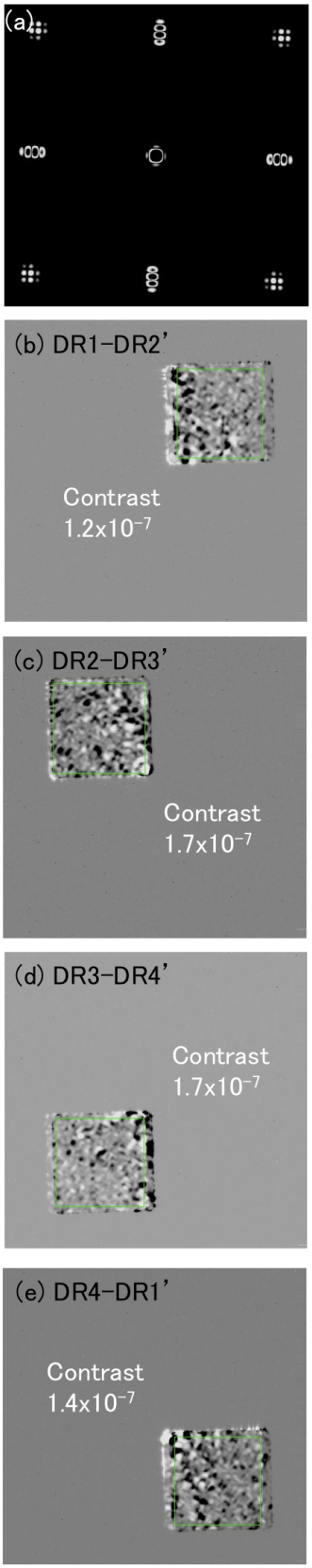

Figure 2.16: Rotated mask subtraction 2: the way in which the image after mask rotation was subtracted from that before mask rotation. Panel (a): shifting the core image before mask rotation to fit the centers of the cores before and after mask rotation. Panel (b), (c), (d) and (e): images of the results of rotated mask subtraction 2 (DR1-DR2', DR2-DR3', DR3-DR4', DR4-DR1').

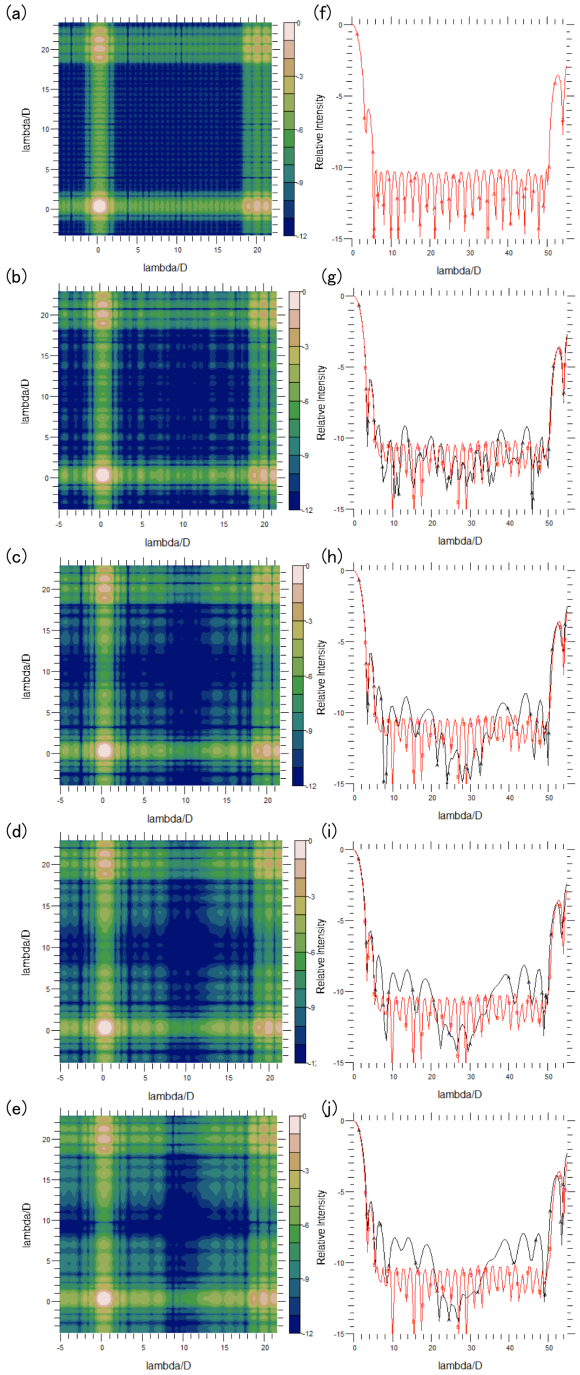

Figure 2.17: Simulated PSFs of the free-standing mask. (a) and (f): Simulated PSFs from the perfect mask. (b) and (g): Simulated PSFs from an across-the-board 5μm increase in the line width of the mask. (c) and (h): Simulated PSFs from an across-the-board10μm increase in the line width of the mask. (d) and (i): Simulated PSFs from an across-the-board 15μm increase in the line width of the mask. (e) and (j): Simulated PSFs from an across-the-board 20μm increase in the line width of the mask. (a), (b), (c), (d) and (e) are simulated images and (f), (g), (h), (i) and (j) are simulated profiles. The red and black lines show the PSFs for the perfect and imperfect masks, respectively. The scale is logarithmic.

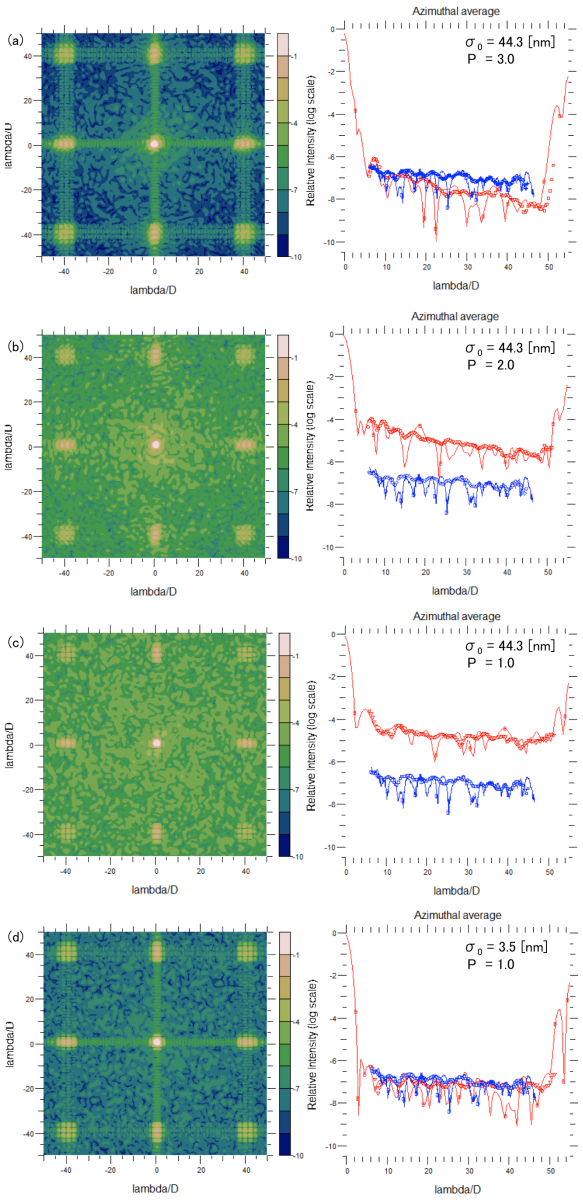

Figure 2.18: Simulated PSFs of the free-standing mask. Left: Simulated PSFs from the PSDs. Right: Diagonal profiles and average azimuthals of the PSFs. The red line shows the PSF profile and the red triangles show the average azimuthals from the simulation. The blue line shows the PSF profile and the blue squares show the average azimuthals from the experiment. (a)σ_0=44.3 nm ($\lambda_0/14$)as the SPICA mirror RMS and p=3.0 as a typical telescope mirror (for example, the HST and the VLT mirror have p=2.9 and p=3.1). The error sum of the squares is 1.6×10^{-12}. (b) Changing p=3.0 to p=2.0. The error sum of the squares is 7.9×10^{-8}. (c) Changing p=2.0 to p=1.0. The slope of the simulation was fit to the slope of the experiment. The error sum of the squares is 1.6×10^{-7}. (d) Changing σ_0=44.3 nm to σ_0=3.5nm. This is the best fit for the experimental PSF. The error sum of the squares is as small as 4.4×10^{-13}.

Second, we discuss the results of Rotated mask subtraction 2 using the result from the WFE simulation. Specifically, we simulated the PSFs from the error in replicating the mask position. We estimated an upper limit for the error due to the mask position. There are two reasons for the error in mask position to occur when the mask is rotated.

1. An error in the position of the mask holder.
   The mask holder has 4 threaded holes for inserting a rod on the left, right, top and bottom. The mask holder, including the position of the threaded holes, has good central symmetry and a high accuracy (< 0.1mm) . The error might include a tilt error ($< 1^\circ$) because of the threaded anchorage. The contribution of the tilt error to the positional error of the mask holder is negligibly-small.

2. The error in position between the mask and the mask holder.
   The mask holder has a mask location allowance. The mask holder is about 1mm larger than the mask in height and width.

Therefore, we assumed the upper limit of the error in replicating the mask position is 1mm and simulated the PSF from the mask position shifted 1mm on the pupil-plane Fig.2.19. We subtracted the PSF after shifting the mask from that before shifting it. Fig.2.19(e) shows the PSF after subtraction. We evaluated the contrast between the standard deviation of the dark region and the peak of the core. As a result, a contrast of 6.3×10^{-8} was obtained. The contrast of 6.4×10^{-8} was not as bad as the contrast (1.2×10^{-7}) after rotated mask subtraction 2. Furthermore, the result (6.4×10^{-8}) was not as bad as the contrast (8.1×10^{-8}) without mask rotation confirming the stability of the optical system. We can see from the above that the error in replicating the mask position is not the main factor after rotated mask subtraction 2.

It is suggested from the above that one of the main factors of the results after rotated mask subtraction 2 is the low stability of the optical system. It was explained qualitatively that the result of rotated mask subtraction 2 gave a poorer contrast of 1.2×10^{-7} than the contrast of 8.1×10^{-8} without mask rotation because a longer time interval between observations is required for rotated mask subtraction 2 than subtraction without mask rotation.

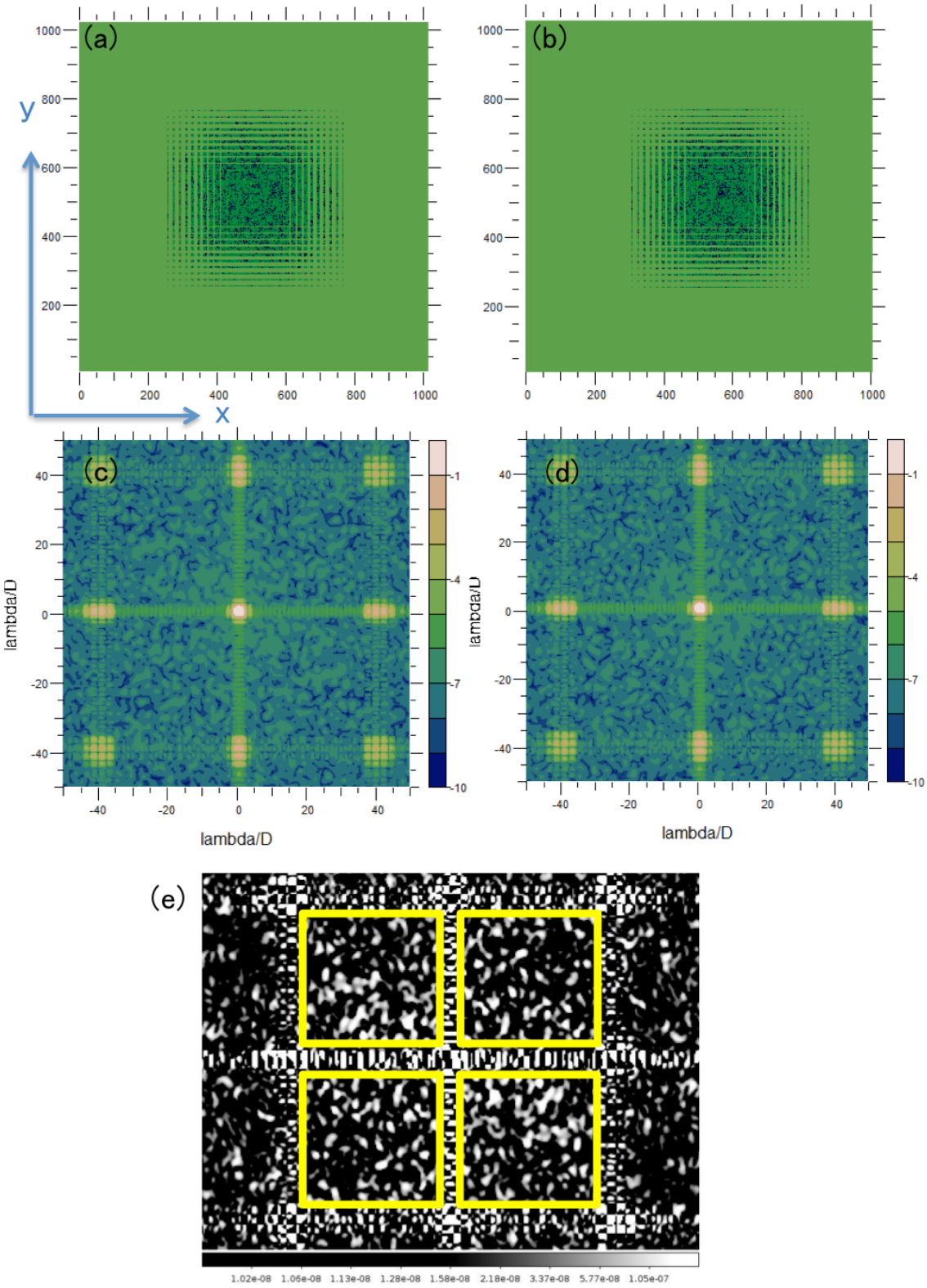

Figure 2.19: Simulated pupil-plane and PSFs. (a): Simulated surface roughness with the binary-shaped pupil mask. (b): Simulated surface roughness with the binary-shaped pupil mask shifted by 1mm in the x-direction. (c): Simulated PSF from (a). (d): Simulated PSF from (b). (e): Image after subtracting (d) from (c). The contrast in the four quadrants (yellow squares) is 6.4×10^{-8}, 6.4×10^{-8}, 6.3×10^{-8}, and 6.4×10^{-8} respectively.

Chapter 3

Discussion

3.1 Merits of the binary-shaped pupil mask coronagraph for actual observations

We carried out a series of studies on the binary-pupil mask in order to address the critical issues for using a binary-shaped pupil mask coronagraph on a telescope for the direct observation of exoplanets. As mentioned in the Introduction, the critical issues are as follows.

1. The WFE caused by imperfections in the optics is an important limiting factor in the contrast of a coronagraph in space telescopes.

2. An actual observation is a multi-color/broadband observation, not a monochromatic observation.

3. A checker-board mask with a glass substrate can cause problems in that there are light transmission losses, ghosting from residual reflectances and a slightly different refractive index for each wavelength.

We discussed three experiments with regard to these issues.

1. As a result of using PSF subtraction, we improved the contrast by around two orders of magnitude from the raw contrast at the He-Ne laser wavelength. We demonstrated that the contrast of a binary-shaped pupil mask coronagraph with PSF subtraction can achieve a contrast of $\sim 10^{-9}$, which is the contrast required to directly observe giant planets. The result confirmed that PSF subtraction of stable images is potentially beneficial for improving the contrast in the laboratory. If enough stability and improvement in contrast as a result of PSF subtraction can be expected during coronagraph observations with SPICA or other telescopes, the requirements for the raw contrast can be significantly relaxed. Thus, the requirements for the static WFE can also be relaxed in a stable environment. This therefore can provide a significant advantage for the development of telescopes.

2. The first results of our demonstration using multi-color/broadband sources have shown that the binary-shaped pupil mask coronagraph produces significant improvement in contrast in various wavelength bands compared with non-coronagraphic optics. This result provide a significant advantage in installing a binary-shaped pupil mask coronagraph in a telescope, because it is necessary to make observations over a wavelength band, and it would be beneficial to make observations using multiple bands for an actual observation.

3. It was demonstrated that a free-standing mask has the capacity to improve the contrast to 1.0×10^{-7}, which was achieved for the raw coronagraphic image by areal averaging of all the observed dark regions. Because a free-standing masks is independent of wavelength it can be use in the infrared region. For instance, it can also be installed in the next-generation infrared telescope SPICA. Nevertheless the mask pattern needs to be changed from a checker-board design to a new mask pattern that takes the pupil shape of the telescope with a secondary mirror and spiders into consideration (Enya & Abe, 2010).

3.2 PSF subtraction at different wavelengths

Since we had multi-color/broadband results, we applied the PSF subtraction at different wavelengths. In principle, PSF subtraction of images at different wavelengths cannot completely remove WFE, even static WFE, because WFE is wavelength dependent. On the other hand, if the wavelength difference is small, the noise pattern is expected to be similar. So we consider that PSF subtraction is effective in practice for improving contrast (e.g., Biller et al. (2009)). We used images at 650nm and 750nm which had only a small amount of ghosting. Because the image size is proportional to λ/D, the image at 650nm was enlarged by 750/650 to make it the same size as the image at 750nm. The positions were aligned by using a bright diffraction pattern outside the dark region as a guide. The intensity was adjusted to the peak of the core image at 750nm. We adjusted the size, position and intensity as described above and subtracted the image at 650nm from the image at 750nm. As a result, the areal mean of the dark region had a positive value. In other words, the dark region for 750nm was brighter than the dark region for 650nm. We believe this is because the ghost image is more pronounced at longer wavelengths. The contrast between the peak of the core at 750nm and the areal mean of the dark region after PSF subtraction was 7.8×10^{-7}. The contrast was a little better than 1.1×10^{-6} which is the raw contrast at 750nm, though the improvement in contrast was not as much as that obtained in the PSF subtraction experiment with the He-Ne laser. Fig.2.9 shows no significant elongated pattern expected from the difference in $\Delta\lambda/\lambda_c$ at 650nm and 750nm. If we use images at longer wavelengths, the ghosting increases. Thus, there is a need for the installation of a mirror optics system to reduce the effects of ghost images.

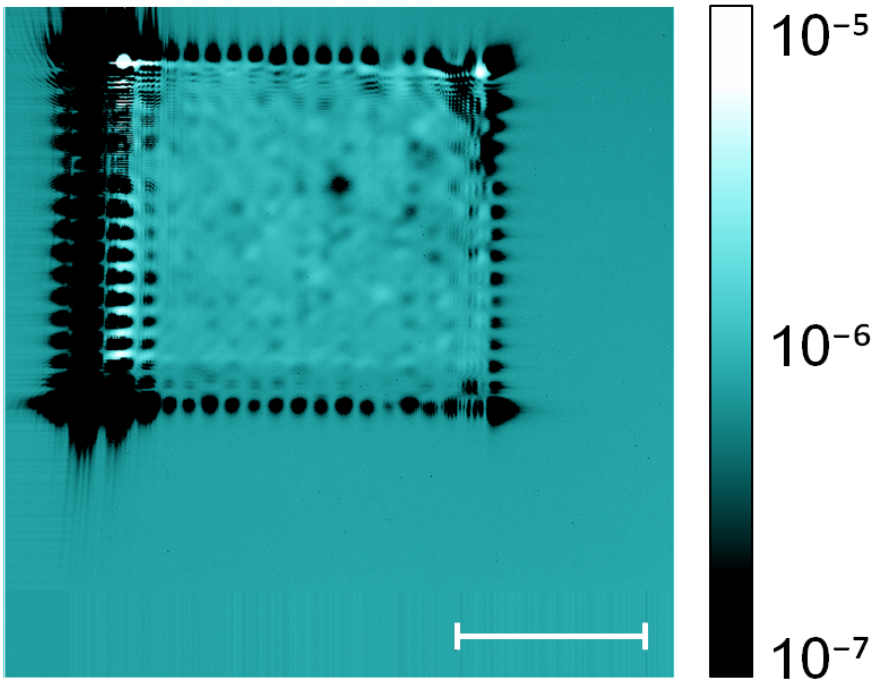

Figure 3.1: An image of the result of PSF subtraction using two raw coronagraphic images at 650nm and 750nm. The scale bar is $10\lambda/D$.

3.3 Comparison with other experiments

A worldwide development race is being conducted (e.g., review in Guyon et al. (2006)). Experimental demonstrations are necessary because the theory is ahead of the experiments, and the experiments conducted need to have a high accuracy to enable the theory to be demonstrated. In this section, we describe the coronagraphic experiments for space-telescopes being carried out worldwide. There are two different types of space-coronagraph; one is focused on the direct observation of light reflected by the exoplanet at visible wavelengths and the other is focused on the direct observation of thermal emissions from the exoplanets at infrared wavelengths.

The Terrestrial Planet Finder Coronagraph (TPF-C) is a coronagraph space mission capable of detecting and characterizing Earth-like planets and planetary systems at visible wavelengths around nearby stars. TPF-C will use spectroscopy to measure key properties of exoplanets including the presence of atmospheric water or oxygen, powerful signatures in the search for habitable worlds. A band-limited (BL) coronagraph was selected for the TPF-C Flight Baseline (FB1) architecture as it is the most mature technique, having been demonstrated in the laboratory to perform at levels needed for detecting Earths, 5.2×10^{-10} at 4 λ/D for 760-840nm (10% band) in natural unpolarized light, thus verifying the fundamental physics and establishing its feasibility (Kern et al., 2008; Trauger & Traub, 2007). Other space missions with similar visions have been proposed, which aim at direct observation of Earth-like exoplanets using off-axis space telescopes and various kinds of coronagraph.

The James Webb Space Telescope (JWST) is a space mission, which has a 6.5 m segmented aperture with four types of instruments, and will be launched in 2014. Several coronagraphs will be installed in JWST: One of the objectives of MIRI, the Mid-InfraRed Instrument of the JWST (5-28 μm), is the direct detection of Extrasolar Giant Planets (EGPs) around young stars (Cavarroc et al., 2008). Four coronagraphs are installed in MIRI. One is a Lyot coronagraph operating at 23 μm optimized for the study of circumstellar disks, the three others are monochromatic FQPMs operating at 10.65 μm, 11.4 μm, and 15.5 μm. They are associated with narrowband filters (the spectral bandpass is 5% for the FQPMs and 20% for the Lyot coronagraph) and are optimized for the detection and characterization of Jupiter-like planets (Boccaletti et al., 2005; Baudoz et al., 2006). It also includes the NIRCam coronagraph between 2.1 μm and 4.6 μm (Krist et al., 2009) and the Non-Redundant Masking on the Fine Guidance Sensor Tunable Filter Imager (FGS-TFI/NRM) between 3.8 μm and 5.5 μm (Sivaramakrishnan et al., 2009).

SPICA (2018 launch planned) is an astronomical mission optimized for mid-infrared and far-infrared astronomy with a 3m class on-axis telescope cooled to <6K (Nakagawa et al., 2010). The primary target of the SPICA coronagraph is self-luminous Jovian exoplanets around 1-5 Gyr old G-M type stars. The

binary shaped pupil mask coronagraph has the potential to be installed as the SPICA coronagraph (Enya et al., 2010).

Next, we refer to laboratory testing for space-telescopes. Several concepts exist, many are being prototyped across the world, and some have already been demonstrated.

Phase Mask laboratory testing: Monochromatic device performance has already been demonstrated and the manufacturing procedures are well-under control since their development. Among them, the Annular Groove Phase Mask (Mawet et al., 2005; Foo et al., 2005), the Four-Quadrant Phase Mask (FQPM) (Carlotti et al., 2009) , and the Eight-Octant Phase Mask (EOPM) (Murakami et al., 2008) are quite promising. The multistage four-quadrant phase mask (MFQPM) reduces the stellar flux over a spectral range and it is a very good candidate to be associated with a spectrometer for future exoplanet imaging instruments on ground- and space-based observatories (Baudoz et al., 2008). The coronagraph gives an average transmission between 7×10^{-6} and 4×10^{-5} at each wavelength over a 20% bandwidth (660-800 nm). (Galicher et al., 2011).

PIAA laboratory testing: The laboratory experiment achieved a 2.27×10^{-7} raw contrast between 1.65 λ/D (inner working angle of the coronagraph configuration tested) and 4.4 λ/D (outer working angle) (Guyon et al., 2010). The NASA Ames Research Center PIAA coronagraph laboratory is a highly flexible testbed operating in air (Belikov et al., 2009). It is dedicated to PIAA technologies and is ideally suited to rapidly developing and validating new technologies and algorithms. It uses MEMS-type deformable mirrors for wavefront control. The NASA JPL High Contrast Imaging Testbed (HCIT) is a highly stable vacuum testbed facility for coronagraphs. PIAA is one of the coronagraphic techniques tested in this lab, which provides the stable vacuum environment ultimately required to validate PIAA for flight (Kern et al., 2009) .

Laboratory testing of a pupil-plane Mask Coronagraph: Belikov et al. (2006) achieved a contrast of 4×10^{-8} using a visible laser, and a contrast of $\sim 10^{-7}$ using a broadband light source with speckle nulling in a small area from $4\lambda/D$ to $9\lambda/D$.

There are many various kinds of coronagraphic experiment which have different purposes and different demonstration performance. The common characteristic of JWST, SPICA, TPF-C and other missions using visible light coronagraphs is that they are space-borne coronagraphs. TPF-C and the visible coronagraph missions are aimed at the direct observation of light reflected by exoplanets (ultimately, Earth-like planets) at visible wavelengths. On the other hand, JWST and SPICA are aimed at the direct observation of thermal emission from exoplanets at infrared wavelengths. A larger entrance aperture

and an earlier launch date are big advantages of JWST. For SPICA, a binary-pupil mask coronagraph, such as used in this study, is suitable, in principle, for spectroscopic observations, because it is effective over a range of wavelengths. Meanwhile, the FQPM and the Lyot coronagraph, which are candidates for the JWST coronagraph, are wavelength dependent. In recent years, however, MFQPMs and apodized-pupil Lyot coronagraphs involving multistage configurations can reduce the stellar flux over a range of wavelengths.

The common feature between the HCIT study and our study is the use of a vacuum chamber. A range of different coronagraphs, such as a binary-pupil mask coronagraph, PIAA and the Lyot coronagraph are being studied on the HCIT. Multi-color experiments with speckle nulling were conducted on the HCIT. On the other hand, in this study, we used only binary-pupil mask coronagraphs. We conducted multi-color/broadband experiments without speckle nulling.

It is beneficial to compare this work with other experiment using a binary-shaped pupil mask coronagraph. Belikov et al. (2006) achieved a contrast of 4×10^{-8} using a visible laser, and $\sim 10^{-7}$ contrast using a broadband light source with speckle nulling in a small area from $4\lambda/D$ to $9\lambda/D$. On the other hand, our experiments in this paper were performed without speckle nulling. The works shown in this paper resulted in a contrast of 2.3×10^{-7} using a He-Ne laser, which is close to the limit of the mask design, and a contrast of $\sim 10^{-6}$ using a broadband source in a larger area, from $3\lambda/D$ to $30\lambda/D$. Therefore, these works are complementary to each other. It is a possible, in future work, for us to introduce speckle nulling in order to reach a higher contrast (Kotani et al., 2010). In such a case, the design of our free-standing mask can be useful because the contrast produced by this mask is designed to be 10^{-10}.

3.4 Future works

There are two ways of developing this work. One is focusing on the direct observation of light reflected by the exoplanet using a space coronagraph at visible wavelengths. This means that the coronagraph must achieve a contrast of 10^{-10} at visible wavelengths. It was found that a major limiting factor for the contrast is the WFE. If proper wavefront control is used in this binary-shaped pupil mask coronagraph experiment, an improvement in contrast is expected. Compared to other previous studies (i.e., HCIT), the raw contrast is very high in this study. It is interesting to pursue higher contrast with the vacuum chamber and wavefront control. The other way of developing this work is to focus on the direct observation of thermal emission from exoplanets using a space coronagraph at infrared wavelengths. This means that the coronagraph must achieve a contrast of 10^{-6} at infrared wavelengths. To achieve this, we must reduce the thermal noise, which requires the application of a cryogenic vacuum chamber. Glass lenses cannot be used and mirror optics are appropriate for infrared experiments. We need infrared sources and an infrared detector. A glass substrate mask cannot be used. The use of a free-standing mask is very promising in this case.

Chapter 4

Summary and Conclusion

The direct detection and spectroscopy of exoplanets is essential for understanding how planetary systems were born, how they evolve, and, ultimately, for finding biological signatures on these planets. The enormous contrast in luminosity between the central star and a planet presents the primary difficulty in the direct observation of exoplanets. For example, if the solar system is observed from a distance, the expected contrast between the central star and the planet is $\sim 10^{-10}$ in the visible light region and $\sim 10^{-6}$ in the mid-infrared region. Therefore, the development of stellar coronagraphs, which can improve the contrast between the star and the planet, is needed. Of the various kinds of coronagraph, we have focused on a binary-shaped pupil mask coronagraph. The reasons for using this coronagraph are that it is robust against pointing errors, it can, in principal, be used to make observations over a wide wavelength range and it is relatively simple. Also, the adoption of a binary-shaped pupil mask coronagraph for SPICA is considered. We conducted a number of coronagraphic experiments in a vacuum chamber using a checkerboard mask, which is a kind of binary-shaped pupil mask, without active wavefront control. This study is unique and important in that it includes not only the tasks necessary to make the coronagraph fit for practical use, but also tests to verify its use for actual coronagraphic observations. The three kinds of experiment carried out for this study are described below.

1. In space telescopes, the WFE caused by imperfections in the optics is an important limiting factor in the contrast of a coronagraph. Subtracting the PSF is beneficial in that it removes any static WFE, and achieves a higher contrast than that in the raw image. Subtraction of the PSF is available in the direct observation of exoplanets using space telescopes, which helps to improve high-contrast observations. We evaluated how much the PSF subtraction contributed to the high contrast observation by subtracting the images obtained through the coronagraph. We improved the temperature stability by installing the coronagraph optics in a vacuum chamber, controlling the temperature of the optical bench, and covering the vacuum chamber with thermal insulation layers. With a He-Ne laser at a wavelength of 632.8nm, a contrast of 2.3×10^{-7} was obtained for the raw coronagraphic image and a contrast of 1.3×10^{-9}

was achieved after subtraction of the PSF. Thus, an improvement of around two orders of magnitude in contrast was achieved by subtracting the PSF.

2. A He-Ne laser was employed as the light source in the previous experiments. On the other hand, the binary-shaped pupil mask coronagraph should, in principal, be used for observations over a wide range of wavelengths. Actual observations are made over a wavelength band, and it would be profitable to make observations using multiple bands. We carried out multi-color/broadband experiments using SLEDs with center wavelengths of 650nm, 750nm, 800nm and 850nm in order to demonstrate the coronagraph's potential for making more realistic observations. We achieved contrasts of 3.1×10^{-7}, 1.1×10^{-6}, 1.6×10^{-6} and 2.5×10^{-6} at the bands centered on 650nm, 750nm, 800nm and 850nm, respectively. We experimentally proved the multi-color/broadband coronagraph.

3. However, the checker-board mask with a glass substrate has the problems of transmission losses, ghosting from residual reflectances and a slightly different refractive index for each wavelength. Therefore, we developed a new free-standing sheet metal mask without the need for a substrate. The free-standing mask can be used for infrared observations which have a great advantage over visible light observations in that the contrast between the star and the planet is much less. In the experiment with the He-Ne laser and the free-standing mask, we achieved contrasts of 9.6×10^{-8}, 9.6×10^{-8}, 9.5×10^{-8} and 1.2×10^{-7} in the DR1, DR2, DR3 and DR4, respectively. Speckles are the major limiting factor. A similar significant improvement in contrast was demonstrated with the free-standing mask as with the substrate mask.

We demonstrated that subtraction of the PSF is potentially beneficial for improving the contrast of a binary-shaped pupil mask coronagraph, that this coronagraph can provide a significant improvement in contrast with multi-color/broadband light sources, and that the new free-standing mask for practical use provides superior performance of improving contrast. We performed the tasks necessary to make the coronagraph fit for practical use. In conclusion, we carried out verification tests on the binary-shaped pupil mask coronagraph for actual coronagraphic observations. In this study we developed the study of the checker-board mask coronagraph and overcame difficulties encountered in practical observations by satellite. Consequently, the results of this study suggest that the binary-shaped pupil mask coronagraph can be applied to coronagraphic observations by SPICA and other telescopes.

Acknowledgements

I am deeply indebted to Professor Matsuhara for giving me the great opportunity to study infrared astronomy at ISAS/JAXA. I thank Professor Nakagawa for his comments on the experiments and this paper. I am grateful to Assistant Professor Enya for his enormous support and insightful comments. His comments and suggestions were of inestimable value for this study. I thank T. Kotani for his advice in carrying out the wavefront simulations. Discussions with L. Abe were very fruitful for this study. I am grateful to the pioneers of the checker-board pupil mask coronagraph, especially R. J. Vanderbei. This research was partially supported by a Grant-in-Aid for JSPS Fellows. The pupil mask was supported by the Nano-Processing Facility of the Advanced Industrial Science and Technology. The Free-standing mask was made with Howa Sangyo Co., Ltd and Photo Precision Co., Ltd. I thank SIGMA KOKI CO., LTD. for providing the BMAR data.

I would like to express my thanks to the members of the department of infrared astrophysics in ISAS/JAXA for their comments, which have made an enormous contribution to my work. I would also like to express my gratitude to my parents and my husband Ryo for their continuing support and warm encouragement.

Bibliography

Abe, L., Vakili, F., & Boccaletti, A. 2001, A&A, 374, 1161

Aime, C., Soummer, R., & Ferrari, A. 2001, A&A, 379, 697

Aime, C. 2005, A&A, 434, 785

Aime, C., & Soummer, R. 2004, Proc. of SPIE, 5490, 456

Baudoz, P., Boccaletti, A., Riaud, P., Cavarroc, C., et al. 2006, PASP, 118, 765

Baudoz, P., Galicher, R., Baudrand, J., & Boccaletti, A., 2008, Proc. of SPIE, 7015, 176

Beaulieu, J.-P., Bennett, D. P., Fouque', P., et al., 2006, Nature, 439, 437

Belikov, R., Giveón, A., Trauger, J. T., et al. 2006, Proc. of SPIE, 6265, 18

Belikov, R., Pluzhnik, E., Connelley, M. S., et al. 2009, Proc. of SPIE, 7440, 17

Bennett, D. P., Bond, I. A., Udalski, A., et al., 2008, ApJ, 684, 663

Biller, B., Trauger, J., et al. 2009, PASP, 121, 881, 716

Boccaletti, A., Baudoz, P., Baudrand, J., Reess, J. M., Rouan, D., 2005, ASR, 36, 1099

Bond, I. A., Udalski, A., Jaroszyski, M., et al., 2004, ApJ, 606, 155

Borde, P., & Traub, W. A., 2006, ApJ, 638, 488

Burrows, A, Sudarsky, D, Lunine, J. I.. 2003, ApJ, 596, 587

Carlotti, A., Ricort, G., & Aime, C., 2009, A&A, 504, 663

Carlotti, A., Vanderbei, R., & Kasdin, N. J., 2011, arXiv:1108.4050

Cavarroc, C., Amiaux, J., Baudoz, P., Boccaletti, A., et al. 2008, Proc. of SPIE, 7010, 29

Charbonneau, D., Brown, T. M., Latham, D. W., & Mayor, M. 2000, ApJ, 529, 45

Codona, J. L., & Angel, R. 2004, ApJ, 604, L117

Deming, D., Seager, S., Richardson, L. J., & Harrington, J. 2005, Nature, 434, 740

Enya, K., Tanaka, S., Abe, L., & Nakagawa, T. 2007, A&A, 461, 783

Enya, K., & SPICA working group, 2010, ASR, 45, 979

Enya, K., & Abe, L. 2010, PASJ, 62, 1407

Enya, K., Abe, L., Takeuchi, S., Kotani, T., & Yamamuro, T., 2011, Proc. of SPIE, in press

Foo, G., Palacios, D. M., & Swartzlander, G. A., Jr., 2005, Opt. Lett., 30, 3308

Galicher, R., Baudoz, P., Baudrand, J., 2011, A&A, 530, 43

Green, J. J., Shaklan, S. B., Vanderbei, R. J., & Kasdin, N. J. 2004, Proc. of SPIE, 5487, 1358

Gonsalves, R., & Nisenson, P. 2003, PASP, 115, 706

Guyon, O. 2003, A&A, 404, 379

Guyon, O., Pluzhnik, E., Galicher, R., et al., 2005, ApJ, 622, 744

Guyon, O., Pluzhnik, E. A., Kuchner, M. J., Collins, B., & Ridgway, S. T., 2006, ApJ, 167, 81

Guyon, O., Pluzhnik, E., Martinache, F., et al.2010, PASP, 122, 71

Guyon, O., & Roddier, F. J. 2000, Proc. of SPIE, 4006, 377

Haze, K., Enya, K., Abe, L., et al. 2009, ASR, 43, 181

Jacquinot, P., & Roizen-Dossier, B. 1964, Prog. Opt., 3, 29

Kalas, P., Graham, J. R., Chiang, E., et al. 2008, Science, 322,1345

Kasdin, N. J., Vanderbei, R. J., Spergel, D. N., & Littman, M. G. 2003, ApJ, 582, 1147

Kasdin, N. J., Belikov, R., Beall, J., Vanderbei, R. J., et al. 2005a, Proc. of SPIE, 5905, 128

Kasdin, N. J., Vanderbei, R. J., Littman, M. G., & Spergel, D. N., 2005b, Appl. Opt., 44, 1117

Kern, B., Belikov, R., Give'On, A., Guyon, O., et al. 2009, Proc. of SPIE, 7440,15

Kern, K & Trauger, 2008, JPL Publication D-60951

Kotani, T., Enya, K., Nakagawa, T., et. al., 2010, Proc. ASP Conference Series, 430, 477

Krist, J. E., Balasubramanian, K., Beichman, C. A., et. al. 2009, Proc. of SPIE, 7440, 28

Kuchner, M. J., Crepp, J., & Ge, J. 2005, ApJ, 628, 466

Kuchner, M. J., & Traub, W. A. 2002, ApJ, 570, 900

Lyot, B. 1939, MNRAS, 99, 580

Marois, C., Macintosh, B., Barman, T., et al. 2008, Science, 322, 1348

Martinache, F., Guyon, O., Pluzhnik, E. A., et al. 2006, ApJ, 639, 1129

Mayor, M., & Queloz, D., 1995, Science, 378, 6555

Mawet, D., Riaud, P., Absil, O., & Surdej, J., 2005, ApJ, 633, 1191

Murakami, N., Uemura, R,. Baba, N., et al., 2008, PASP, 120, 1112

Nisenson, P., & Papaliolios, C. 2001, ApJ, 548, L201

Nakagawa, T., & SPICA team, 2010, Proc. of SPIE, 7731, 18

Palacios, D. M. 2005, Proc. of SPIE, 5905, 196

Pluzhnik, E. A., Guyon, O., Ridgway, S. T., et al., 2006, ApJ, 644, 1246

Roddier & Roddier, 1997, PASP, 109, 815

Rouan, D., Riaud, P., Boccaletti, A., Clenet, Y., Labeyrie, A., 2000, PASP, 112, 1479

Sidick, E., 2009, Proc. of SPIE, 7390,

Sivaramakrishnan, A., Tuthill, P., Martinache, F., et al., 2009, Astro2010, 40

Soummer, R., Aime, C., & Falloon, P. E. 2003, A&A, 397, 1161

Spergel, D. N. 2001, Astro-ph/0101142

Swain, M. R., Tinetti, G., et al., 2009, ApJ, 704, 1616

Swartzlander, G. A., Jr. 2006, Opt. Lett., 31, 2042

Tanaka, S., Enya, K., Abe, L., Nakagawa, T., & Kataza, H.2006, PASJ, 58, 627

Tinetti, G., Vidal-Madjar, A., 2007, Nature, 448, 169

Traub, W. A., & Jucks, K. W., 2002, Astro-ph/0205369

Traub, W. A., & Vanderbei, R. J. 2003, ApJ, 599, 695

Trauger, J. T., & Traub, W. A. 2007, Nature, 446, 771

Vanderbei, R. J. 1999, Optimization methods & software, 11, 485

Vanderbei, R. J. 2006, ApJ, 636, 528

Vanderbei, R. J., Spergel, D. N., & Kasdin, N. J. 2003a, ApJ, 590, 593

Vanderbei, R. J., Spergel, D. N., & Kasdin, N. J., 2003b, ApJ, 599, 686

Vanderbei, R. J., Kasdin, N. J., & Spergel, D. N. 2004, ApJ, 615, 555

Vanderbei, R. J., & Traub, W. A. 2005, ApJ, 626, 1079

Yang, W., & Kostinski, A. B. 2004, ApJ, 605, 892

Appendix

This section shows the manufacturing process for 10mm size checkerboard masks; masks on silicon, germanium and BK7 substrates, and free standing mask of Cu and Ni. Of these masks, one free standing mask made of Cu was used in the experiments described in this thesis. The Si and Ge masks are for mid-infrared tests in the future, and the BK7 masks are for comparison (they can be conveniently tested with visible light). Free standing masks are also contenders for infrared coronagraphs. All these masks have the same size and same design in order that systematic tests and comparisons for infrared coronagraphs in future.

(The mask with a glass substrate evaluated in this thesis was 2mm in size, so different to the BK7 masks described in this appendix).

A more detailed process of the manufacture is shown below. First, the photomask was manufactured. This photomask was used for all 10mm size masks. Next, the manufacturing process for the masks on Si, Ge, and BK7 substrates, and the manufacturing process for free standing masks of Cu and Ni are shown.

Whilst the main purpose of these masks is for tests for a mid-infrared coronagraph like SPICA, it is also interesting that some of these masks have potential for use in the near infrared and visible wavelength regions.

Fabrication process of a photomask for microstructure patterning

1. 4-inch (101.6mm) square glass substrates are used.
2. Sputtering of $Cr{+}Cr_2O_3$ (0.1 μm thickness) on the substrate (Sputtering is a process for coating substrates with a fine layer of metal, whereby atoms are ejected from a solid target material due to bombardment of the target by energetic particles.)
3. Spin coat resist on Cr_2O_3 with a thickness of 0.5 μm (Spin-coating is a procedure used to make uniform thin layers on flat substrates by rotating the substrate at high speed in order to spread the fluid by centrifugal force)
4. Exposure: draw the microstructure patterns with a 412 nm laser. Development: Remove the photoresist (positive type)
5. Wet etching of the substrate in a acid etch solution in a thin polyvinyl container
6. Strip the resist with a remover

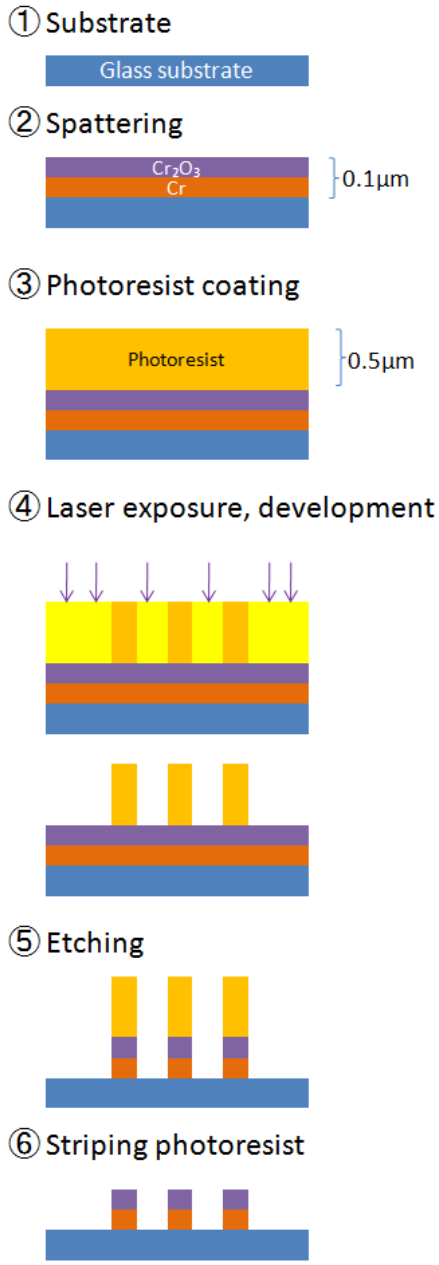

Figure 4.1: Fabrication process of a photomask for microstructure patterning

Fabrication process for masks on BK7 glass, Silicon, and Germanium substrates

1. ϕ 30mm glass substrate, 50mm-square Silicon and Germanium substrate are used
2. EB vapor deposition of aluminum on the substrates with thicknesses of 1000 Å, 2000 Å, 4000 Å, 8000 Å, and 1.6 μm (EB vapor deposition is a type of vapor deposition in which the heating is done by an Electron Beam)
3. Spin coat of photoresist on Al with a thickness of 1 μm
4. Exposure: transfer the patterns from the photomask to the photoresist by UV light (365nm). Development: Remove the photoresist (positive type)
5. Wet etching of the substrate in a acid etching solution in a thin polyvinyl container
6. Strip the photoresist by dipping in acetone

Fabrication process of Cu and Ni free-standing masks

1. Sputtering of $Cr+Cr_2O_3$ (0.1 μm thickness) on 4-inch (101.6mm) square glass substrates. Spin-coat resist (a commercially available one with good surface accuracy) on the glass substrate. Remove the resist and $Cr + Cr_2O_3$ in order to use only the glass substrate
2. Spin-coat a mold releasing agent with a thickness of 1 μm on the surface
3. EB vapor deposition of Cu (0.5 μm thickness) on the releasing agent
4. Spin-coat resist (with a goal of 10 μm thickness) for plating on the Cu substrate
5. Exposure: transfer the patterns from the photomask to the photoresist by UV light (365nm). Development: Remove the photoresist (only the illuminated part is resolved, i.e. positive type resist)
6. Electrolytic plating of Cu with goal thicknesses of 2, 5, 10, 20 μm. 0.5 μm thickness Cu is used as a seed layer for the plating process (Electrolytic plating is a plating process in which metal ions in a solution are moved by an electric field to coat an electrode. The process uses direct electrical current to transfer the positive ions of the desired material from the solution to a conductive electrode (here it is the seed layer) and thereby coat it with a thin layer of the material).
7. Laminate the dry film resist (100 μm thickness) in order to plate the outer support region) after microstructure plating

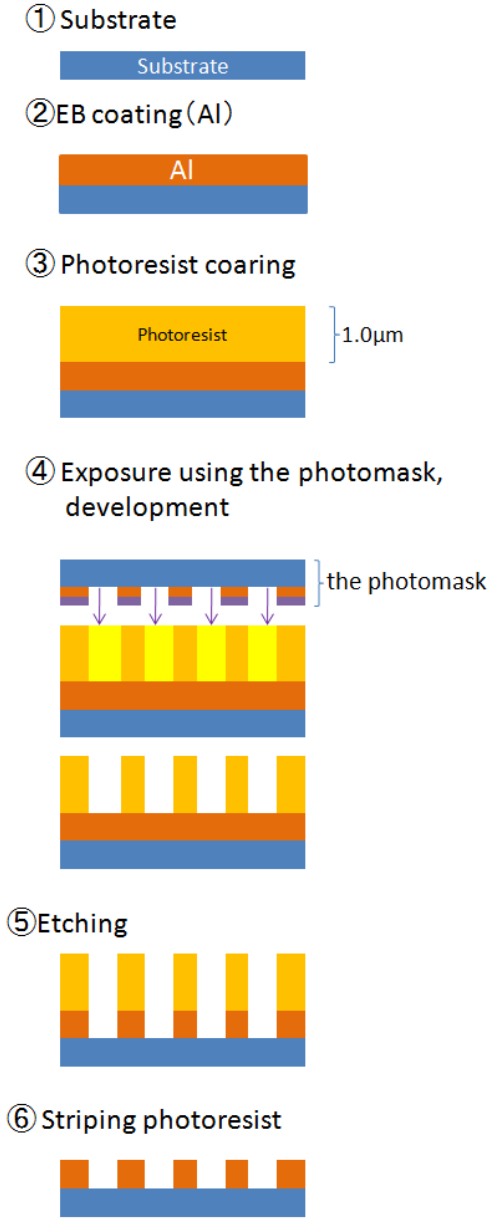

Figure 4.2: Fabrication process of a mask on a BK7 glass substrate. The same processes were applied for other substrates.

8. Exposure: transfer the patterns from the photomask to the photoresist by UV light (365nm). Development: Remove the resist. Only the illuminated part of the dry film resist remains (negative type resist)

9. Electrolytic plating of Cu with a goal thickness of 100 μm. 0.5 μm thick Cu is used for the seed layer

10. Strip the dry film resist by dipping in acetone

11. Strip the resist by dipping in acetone

12. Etch the Cu seed layer (0.5 μm thickness). Wet etch the substrate in an acid etch solution in a thin polyvinyl container. Not only the seed layer but also the 0.5 μm Cu layer is etched and removed

13. Strip the releasing agent in the number 2 by dipping in acetone

14. Rinse the substrate with IPA (isopropyl alcohol) then dry naturally

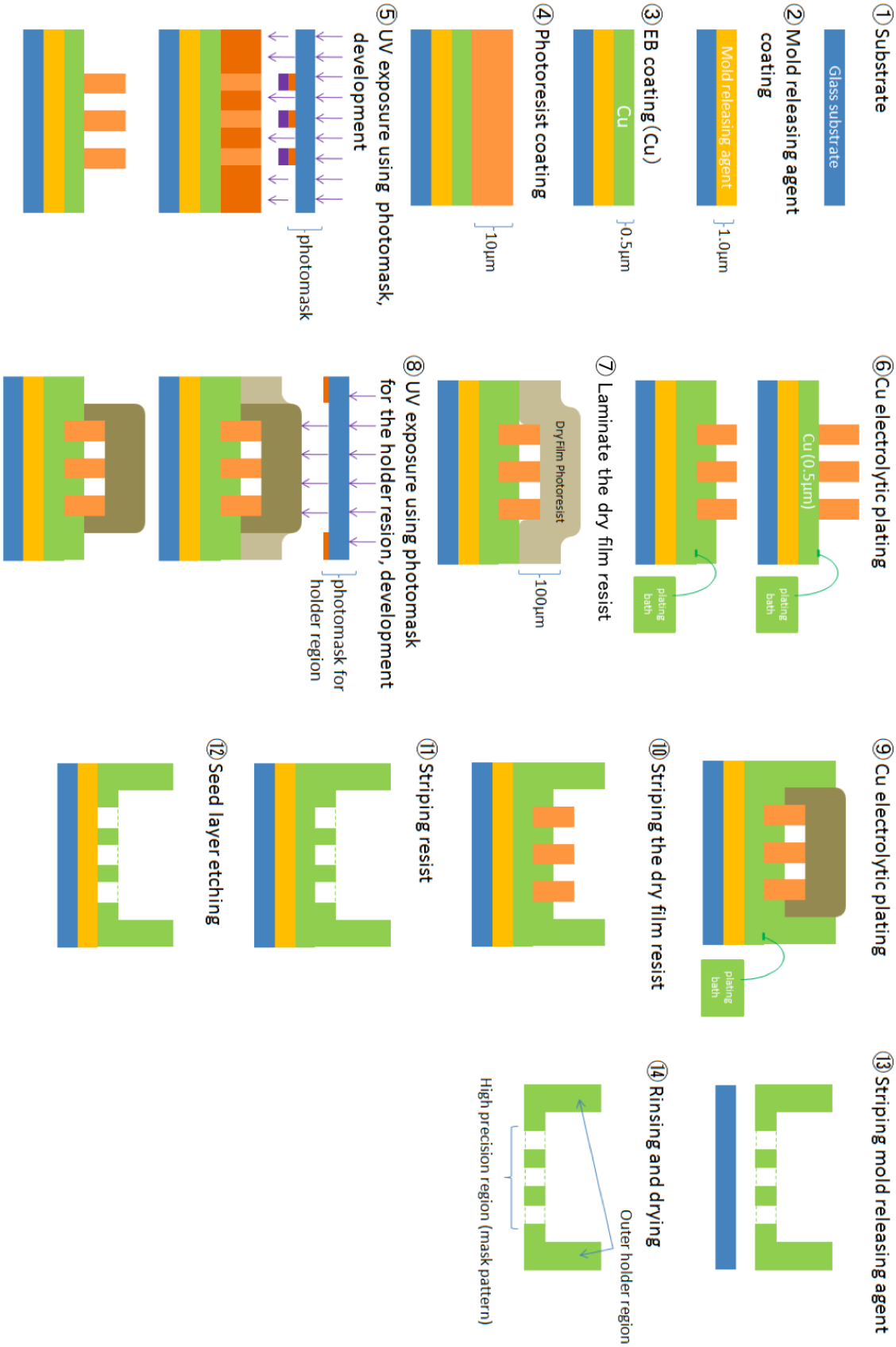

Figure 4.3: Fabrication process of free-standing Cu masks. The same process was applied for free-standing Ni masks.